Analytical Modeling and Controller Design of a Modular Series Parallel Resonant Converter System for a Solid State 2.88-MW/115-kV Long Pulse Modulator

Michael Jaritz, *Member, IEEE*, Tobias Rogg, and Juergen Biela, *Senior Member, IEEE*

***Abstract*—In this paper, two control strategies for voltage balancing in a modular serial parallel resonant converter modulator system, which is used in a high-voltage-pulsed power application, are presented and verified by simulations and measurements. The system is based on two series parallel resonant converter modules, forming an input series output parallel stack. To obtain the given output voltage pulse of 115 kV, nine of these input series output parallel stacks are connected in parallel at the input and in series at the output, forming an input parallel output series system. A robust input voltage balancing by an auxiliary circuit and an output voltage balancing by control is introduced and proven by measurements. In addition, an alternative approach, where the input and output voltage balancing is achieved purely by control, is given and verified by simulations. For designing the control of this system, a large and a small signal model is derived and the influence of component tolerances is investigated.**

***Index Terms*—Input parallel output series (IPOS) control, input series output parallel (ISOP), large signal model, series parallel resonant converters (SPRC) modulator system.**

I. Introduction

MANY enhanced fundamental physic experiments, like the investigation and development of new basic materials, are performed with the help of linear colliders or spallation sources. Medium and high beta cavities used in such linear colliders/spallation sources are supplied by klystron amplifiers or inductive output tube amplifiers. The cathode voltage for these amplifiers can be generated with long pulse modulators generating high-voltage pulses with pulse lengths in the range of milliseconds. With existing modulator topologies all the demanding requirements like a fast pulse rise time, a low-voltage ripple and a long pulse length can hardly be satisfied at the same time in a compact way. For example conventional concepts like bouncer modulator topologies [1], [2] using pulse transformers become huge for long pulses since the volt-seconds of the pulse are high.

Series parallel resonant converters (SPRCs) avoid this drawback as the transformer is operated at high frequencies. Based on the optimization procedure presented in [3], an SPRC-base module [4], [5] has been designed (see Fig. 1) for the specifications of the long pulse modulator for electrical sheet steel given in Table I. There, two SPRC-Bms form an input series output

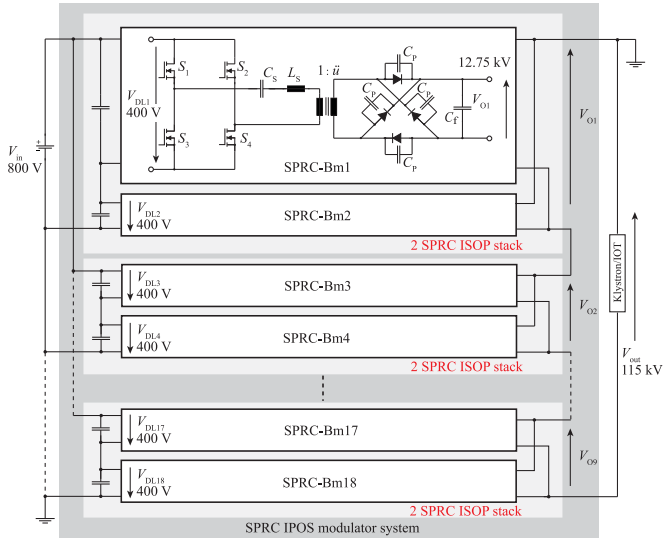

Fig. 1. SPRC modulator system with two SPRC-Bms forming an ISOP stack and nine of them are connected to an IPOS system.

TABLE I
Pulse Specifications

Pulse voltage	V_K	−115 kV
Pulse current	I_K	25 A
Pulse power	P_K	2.88 MW
Pulse repetition rate	P_{RR}	14 Hz
Pulse width	T_P	3.5 ms
Pulse duty cycle	D	0.05
Pulse rise time (0..99% of V_K)	t_{rise}	150 μs
Pulse fall time (100..10% of V_K)	t_{fall}	150 μs

Manuscript received October 31, 2017; accepted December 13, 2017. Date of publication December 19, 2017; date of current version July 15, 2018. This work was supported by CTI and Ampegon AG under CTI-research project 13135.1 PFFLR-IW. Recommended for publication by Associate Editor M. Saeedifard. *(Corresponding author: Michael Jaritz.)*

M. Jaritz and T. Rogg are with D-ITET HPE, ETH Zürich, Zürich 8092, Switzerland (e-mail: mi.jaritz@gmail.com; roggt@hpe.ee.ethz.ch).

J. Biela is with IT & EE, ETH-Zürich, Zürich 8092, Switzerland (e-mail: jbiela@ethz.ch).

Color versions of one or more of the figures in this paper are available online at http://ieeexplore.ieee.org.

Digital Object Identifier 10.1109/TPEL.2017.2785128

parallel (ISOP) stack. The 400 V inputs are connected in series to share the 800 V input supply voltage, which gives the advantage to use commercial off-the-shelf 650 V break down voltage silicon MOSFET switches for the full bridges. The presented control approach, however, is generally applicable. The outputs of the two modules are connected in parallel, resulting in a lower current stress and, therefore, lower losses in the semiconductors and the resonant tanks of each SPRC-Bm. To generate the full system negative pulse voltage and provide the power given in Table I, nine of these ISOP stacks are connected in parallel at the input and in series at the output, forming an input parallel output series (IPOS) system (see Fig. 1). Besides the crucial design of the transformer regarding the isolation design (presented in [6]) and the thermal design (presented in [7]), the control of the IPOS system with an embedded ISOP system is a major challenge, which is the focus in this paper.

In the literature, several possibilities to control ISOP systems exist, as for example like the common duty ratio control [8], the charge control method for a two module ISOP system [9], or the three loop control method [10]. These methods are either working properly only for well-matched SPRC-Bms with small component tolerances, are relatively complicated, or require three control loops. The methods presented in [11]–[13] overcome these problems and present an easily implementable strategy, which requires just two control loops for pure ISOP systems.

In contrast to ISOP systems, equal power sharing, respectively equal output voltage sharing (OVS) has to be achieved for pure IPOS systems as presented in [12]–[15].

The tasks of a proper input/output voltage balancing, as well as an equal power distribution between the SPRC-Bms of the combination of an IPOS system with an embedded ISOP system are not addressed by the methods given in [11]–[15].

In addition, in the combined IPOS-ISOP system, the input/output voltage droop due to the high power consumption during the pulse also has to be compensated, since the energy during the pulse is only provided by the dc-link capacitors.

In order to overcome this problem, the common large signal model of a single SPRC-Bm is extended in this paper, so that also changing dc-link voltages can be considered. Based on this new model, two control strategies for the entire modulator system are presented and verified by simulations as well as measurements.

In addition, an auxiliary circuit for input voltage sharing (IVS) and a new method for balancing the output voltage by controlling the resonant current are presented and verified by measurements. Using the resonant currents instead of the output voltages as control variable for the output voltage balancing enables to avoid the measurement of the output voltage, so that no high-voltage isolated measurement equipment is needed for the voltage balancing. An alternative, also a method, where the input and output balancing is achieved only by control, is described and verified by simulations.

Furthermore, all large signal system and coupling equations, as well as the small system matrices for the IPOS system with an embedded ISOP system are given analytically. This representation can be used to investigate IPOS systems with an arbitrary number of ISOP systems in series, which are formed by an arbitrary number of SPRC-Bms in parallel.

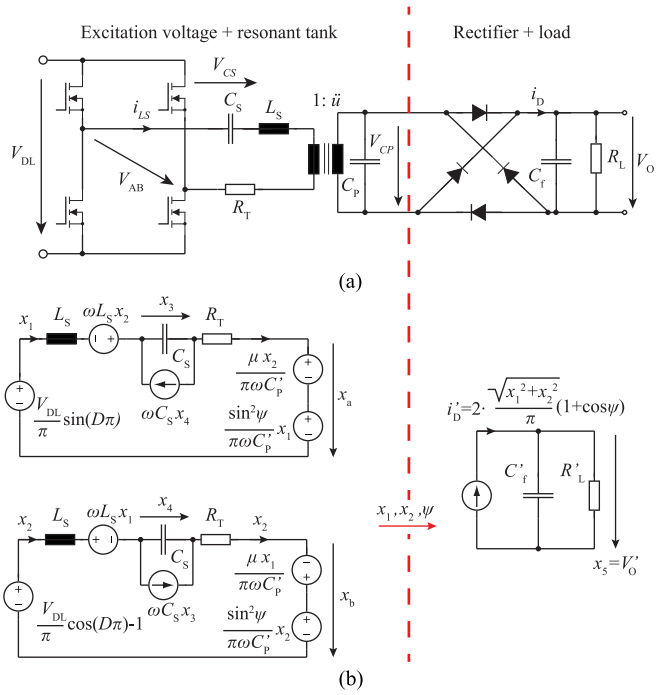

Fig. 2. (a) Switched SPRC-Bm module model. (b) Large signal model of a single SPRC module. The left side represents the excitation voltage and the resonant tank and the right side represents the rectifier and the load.

First, in Section II of this paper, the large and the small signal model of an IPOS system are derived. The proposed control systems are presented in Section III. In addition, component tolerances and their influences on the modulator behavior are discussed. Afterward, measurement and simulation results of the controlled IPOS system are given in Section IV. The detailed derivation of the large signal and the small signal model for the IPOS system is given in Appendix A. All transfer functions used for the controller designs are derived in Appendix B.

II. Large and Small Signal Model of the IPOS System With Embedded ISOP Systems

In this section, the large signal model of an SPRC-Bm is derived. Based on this model, the large signal model of the IPOS system with embedded ISOP systems is presented. Thereafter, the transition to the small signal model is discussed. There, the following definitions are made: V_{O} is used for the output voltage of an SPRC-Bm and V_{out} is used for the output voltage of the IPOS system.

A. Large Signal Model

A detailed derivation of the large signal model of the SPRC-Bm is given in [16]–[18], but for the sake of completeness, the derivation is shortly summarized below.

1) Large Signal Model of an SPRC-Bm: Applying Kirchhoff's law to the SPRC-Bm in Fig. 2(a) results in following nonlinear set of (1), where all magnitudes and components of the secondary transformer side are transferred to the primary ($R'_{\mathrm{L}} = R_{\mathrm{L}}/\ddot{u}^2, C'_{\mathrm{f}} = C_{\mathrm{f}}\ddot{u}^2, C'_{\mathrm{P}} = C_{\mathrm{P}}\ddot{u}^2, V'_{\mathrm{O}} = V_{\mathrm{O}}/\ddot{u}, i'_{\mathrm{D}} = i_{\mathrm{D}}\ddot{u}$, $V'_{CP} = V_{CP}/\ddot{u}$). The definitions of all parameters and compo-

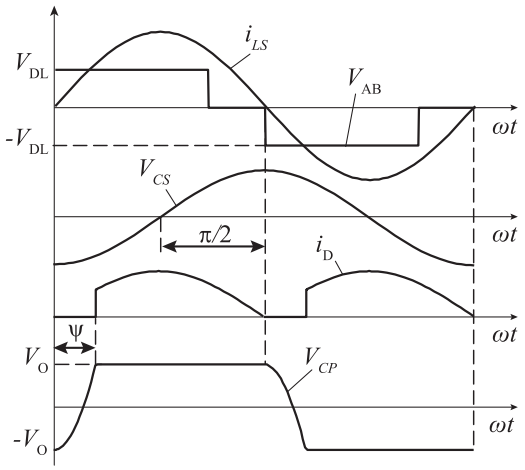

Fig. 3. Basic voltage and current waveforms of an SPRC-Bm according to Fig. 2(a).

nents are given in Figs. 2(a) and 3

$$V_{\mathrm{AB}}(t) = V_{CS}(t) + V'_{CP}(t) + L_{\mathrm{S}}\frac{\mathrm{d}i_{LS}(t)}{\mathrm{d}t} + R_{\mathrm{T}}i_{LS}(t) \tag{1a}$$

$$\frac{\mathrm{d}V_{CS}(t)}{\mathrm{d}t} = \frac{1}{C_{\mathrm{S}}}i_{LS}(t) \tag{1b}$$

$$i'_{\mathrm{D}}(t) = C'_{\mathrm{f}}\frac{\mathrm{d}V'_{\mathrm{O}}(t)}{\mathrm{d}t} + \frac{V'_{\mathrm{O}}(t)}{R'_{\mathrm{L}}}. \tag{1c}$$

It can be seen from (1) that there are six independent variables (i.e. i_{LS}, V_{CS}, V_{CP}, V_{AB}, V_{O}, i_{D}) but just three equations. Therefore, additional relationships have to be found to solve the equation system. In case of the SPRC-Bm, the main waveforms in Fig. 3 are described with the extended describing function [19]. This means i_{LS}, V_{CS}, and V_{AB} can be represented by their first harmonic terms, i.e., the fundamental term of the Fourier series. The output voltage V_{O} and the rectifier current i_{D} are represented by their dc Fourier coefficient with sufficient accuracy [20]. This results in the equation set in (2) and its circuit representation in Fig. 2(b). In this notation the large signal (2) can be easily solved by numerical solvers as the Runge Kutta algorithm and the circuit in Fig. 2(b) can be directly implemented in a circuit simulation program like SPICE

$$\dot{x_1} = \frac{1}{L_{\mathrm{S}}}\left(\frac{V_{\mathrm{DL}}}{\pi}\sin(D\pi) - R_{\mathrm{T}}x_1 - x_3 - x_{\mathrm{a}} + \omega L_{\mathrm{S}}x_2\right) \tag{2a}$$

$$\dot{x_2} = \frac{1}{L_{\mathrm{S}}}\left(\frac{V_{\mathrm{DL}}}{\pi}[\cos(D\pi) - 1] - R_{\mathrm{T}}x_2 - x_4 - x_{\mathrm{b}} - \omega L_{\mathrm{S}}x_1\right) \tag{2b}$$

$$\dot{x_3} = \frac{1}{C_{\mathrm{S}}}x_1 + \omega x_4 \tag{2c}$$

$$\dot{x_4} = \frac{1}{C_{\mathrm{S}}}x_2 - \omega x_3 \tag{2d}$$

$$\dot{x_5} = -\frac{x_5}{R'_{\mathrm{L}}C'_{\mathrm{f}}} + \frac{2\sqrt{x_1^2 + x_2^2}}{\pi C'_{\mathrm{f}}}[1 + \cos(\psi)] \tag{2e}$$

$$x_{\mathrm{a}} = \frac{1}{\pi C'_{\mathrm{p}}\omega}(x_1\sin(\psi)^2 + x_2\mu) \tag{2f}$$

$$x_{\mathrm{b}} = \frac{1}{\pi C'_{\mathrm{p}}\omega}(x_2\sin(\psi)^2 - x_1\mu) \tag{2g}$$

$$\cos\psi = 1 - \frac{x_5 C'_{\mathrm{p}}\omega}{\sqrt{x_1^2 + x_2^2}} \tag{2h}$$

$$\mu = \psi - \sin(\psi)\cos(\psi). \tag{2i}$$

Employing state-space theory on (2) directly results in the state vector $x(t)$ and the input vector $u(t)$ that are used for the controller design

$$x(t) = \begin{bmatrix} x_1 & x_2 & x_3 & x_4 & x_5 \end{bmatrix}^T \tag{3}$$

$$u(t) = \begin{bmatrix} D & \omega & V_{\mathrm{DL}} \end{bmatrix}^T \tag{4}$$

where x_1, x_2 are currents, x_3, x_4, x_5 are voltages, D is the duty cycle, ω is the angular switching frequency and V_{DL} is the dc-link voltage, respectively. The definitions of the elements of the $x(t)$ and $u(t)$ vectors is given in Fig. 4. It is worth mentioning that V_{CP} is not used as state-space variable due to the fact that its signal form in Fig. 3 is neither sinusoidal nor differentiable without case distinctions. However, its influence on the system is fully described with (2f) and (2g) and leads to a reduction of the order of the system by 2. Based on the derived equations, the large signal model for the IPOS system is derived in the following.

2) Large Signal Model of the IPOS System: For the sake of simplicity, the following investigations are performed for a reduced IPOS system as shown in Fig. 4(a) and its corresponding large signal model in Fig. 4(b). It is easily extendable to the full system and also the reduced system provides the conditions for a valid controller design. Fig. 4(a) shows the principle block diagram of the IPOS system, where two modules connected in parallel at the output and in series at the input forming a serial input parallel output system (ISOP). Furthermore, two of the ISOP systems are connected in series at the output and in parallel at the input forming a parallel input series output system (IPOS). Connecting nine of these ISOP systems in series leads to the IPOS modulator depicted in Fig. 1. The input charging unit [IVCU, see Fig. 4(a)] is not able to keep the input voltage constant, due to the high output power during the pulse. Therefore, for the ISOP system, the influence of the variable input voltage of each SPRC-Bm has to be considered additionally. This means that the input variable V_{DL} is described by a new state variable leading to an additional state-space equation for each SPRC-Bm. The variable input voltage is modeled so that the input to output power equilibrium is fulfilled ($R_{\mathrm{T}} \ll$)

$$P_{\mathrm{out}} = P_{\mathrm{in}} \quad \longrightarrow \quad i'_{\mathrm{D}}x_5 = x_{10}i_{C_{\mathrm{DL}}} \tag{5}$$

$$\frac{dx_{10}}{dt} = \frac{1}{C_{\mathrm{DL1}}}\frac{x_5 i'_{\mathrm{D}}}{x_{10}} \tag{6}$$

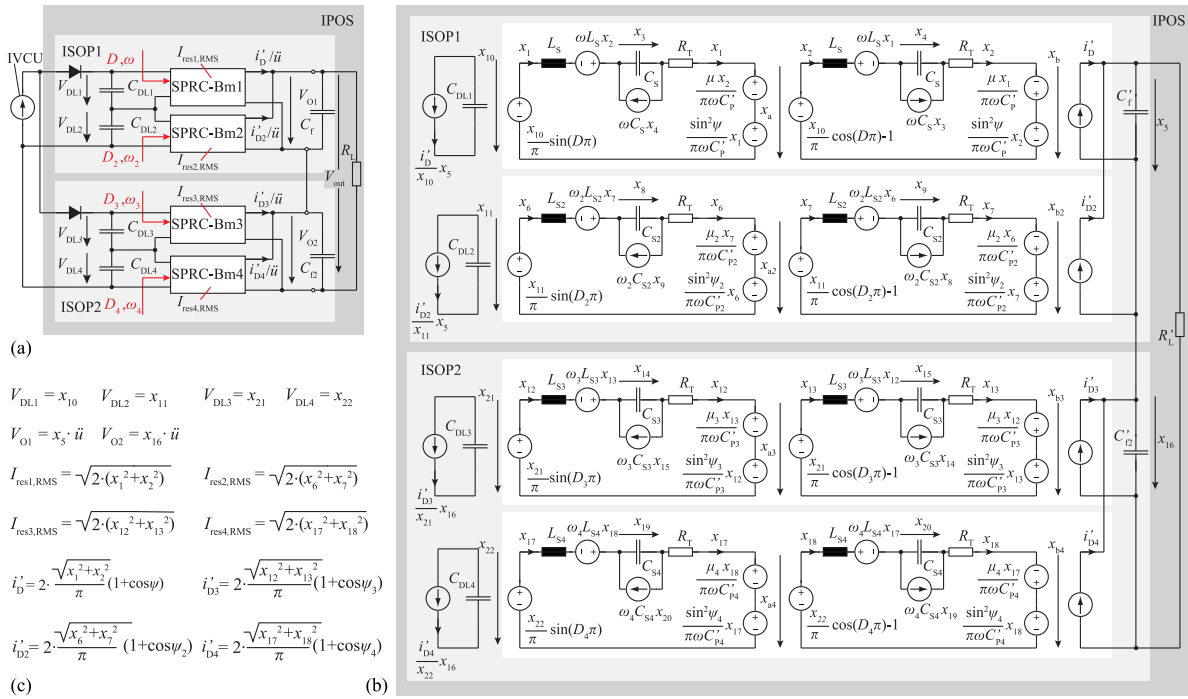

Fig. 4. (a) Block diagram of the reduced IPOS system with embedded ISOP systems and the IVCU. (b) Large signal model of the reduced IPOS system with variable input voltage. (c) Linking definitions between (a) and (b).

where x_{10} represents the input voltage. Finally, the new state and input vectors of the reduced IPOS system are

$$x(t) = \begin{bmatrix} x_1 & x_2 & \cdots & x_{22} \end{bmatrix}^T \tag{7}$$

$$u(t) = \begin{bmatrix} D & \omega & D_2 & \omega_2 & D_3 & \omega_3 & D_4 & \omega_4 \end{bmatrix}^T. \tag{8}$$

All variables of the new state and input vectors can be identified in Fig. 4(b). The complete set of equations and dependencies of the series connection of the reduced IPOS system is given in Appendix A. The simulated output voltages and resonant currents from the switched model match well with the calculated large signal values as depicted in Fig. 5, where the output voltage V_{out} from the large signal model shows the mean value of the switched model and the large signal resonant current gives the envelopes of the switched system. The IVCU is inactive and the used simulation parameters are given in Table II. The dc-link capacitors $C_{\text{DL1}} - C_{\text{DL4}}$ are precharged to $x_{10,\text{init}} - x_{22,\text{init}}$. The derivation of the small signal model is given in the next section.

B. Small Signal Model

For determining the small signal model of the reduced IPOS system a valid operation point has to be calculated. Therefore, all equations in Appendix A are solved until a certain point of time to obtain the operation point values of the state variables (see Table V). By employing the well-known Taylor series to the nonlinear large signal equations around the chosen operation point, the linearized state-space model is derived

$$\begin{aligned} \Delta\dot{x} &= \mathbf{A}\Delta x + \mathbf{B}\Delta u \\ \Delta y &= \mathbf{C}\Delta x + \mathbf{D}\Delta u \end{aligned} \tag{9}$$

where **A**, **B**, **C**, and **D** are the matrices that describe the system, y is the output vector, and Δ is the small change around the operation point [20]. After linearization and applying the Laplace transformation all transfer functions between inputs and state variables can be obtained using

$$\mathbf{G}(s) = \mathbf{C}(s\mathbf{I} - \mathbf{A})^{-1}\mathbf{B} + \mathbf{D}. \tag{10}$$

The small signal transfer functions can be validated by superimposing a small perturbation (approximately 5% of the actual nominal value, [17]) to the duty cycle and/or the switching frequency of the large signal model and by performing an ac analysis over a certain perturbation frequency range. The linearized small signal transfer functions match well with the measured small signal transfer functions, if the perturbation frequency is maximal 20% of the nominal switching frequency, as it has been shown in [17]. It is worth mentioning that the resulting transfer function matrix $\mathbf{G}(s)$ is only valid in the region close to the chosen operation point and has to be recalculated if another operation point is in the scope of interest.

III. Control of an IPOS System With Embedded ISOP Systems

The output voltage V_{out} of the resonant modulator system can be controlled by the duty cycle D and/or by the frequency f [21]. Due to the high-pulsed output power of 159.75 kW of a single SPRC-Bm, the input voltage charging unit is not able to keep the dc-link voltage V_{DL} constant during the pulse. This results in an input and consequently also in an output voltage droop that has to be compensated.

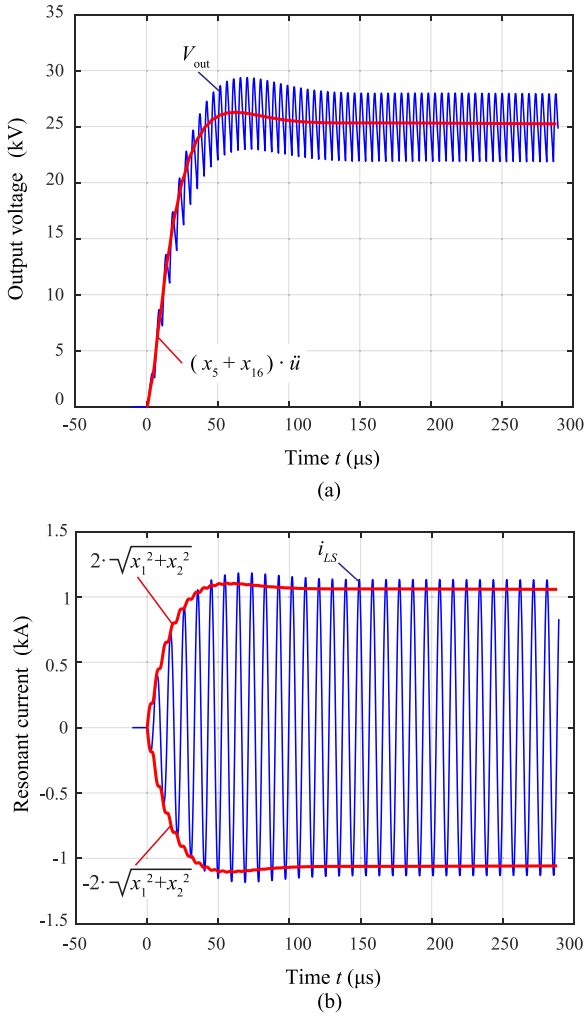

Fig. 5. Comparison of the output voltages and resonant currents between the analytical large signal model (red) [see Fig. 4(b)] and its related simulated switched signal model (blue) of the IPOS system with variable input voltage. The output voltage of the large signal model corresponds to the mean value of the output voltage V_{out} of the switched model. The resonant current of the large signal model corresponds to the peak current values of the switched system resonant current i_{LS}. The IVCU is inactive and the used simulation parameters are given in Table II. The dc-link capacitors $C_{\text{DL1}} - C_{\text{DL4}}$ are precharged to $x_{10,\text{init}} - x_{22,\text{init}}$.

TABLE II
COMPONENT VALUES OF THE SPRC BMS OF AN IPOS SYSTEM WITH VARIABLE INPUT VOLTAGE

Bm1	Bm2	Bm3	Bm4		
Component and input values					
L_{S}	L_{S2}	L_{S3}	L_{S4}	(μH)	4.199
C_{S}	C_{S2}	C_{S3}	C_{S4}	(nF)	840
C'_{P}	C'_{P2}	C'_{P3}	C'_{P4}	(μF)	1.696
R_{T}	R_{T}	R_{T}	R_{T}	(Ω)	0.01
C'_{f}		C'_{f2}		(μF)	8
	R'_{L}			(Ω)	2.875
C_{DL1}	C_{DL2}	C_{DL3}	C_{DL4}	(mF)	30
ω	ω_2	ω_3	ω_4	(krad/s)	$2 \cdot \pi \cdot 106$
D	D_2	D_3	D_4	($-$)	0.8
$x_{10,\text{init}}$	$x_{11,\text{init}}$	$x_{21,\text{init}}$	$x_{22,\text{init}}$	(V)	400

The voltage drop of V_{out} and the influence of component tolerances are discussed first. Afterward, a detailed investigation concerning input and output voltage balancing methods is presented.

A. Voltage Droop Compensation/Component Tolerances

1) Voltage Droop Compensation: Fig. 6(a) (output voltage versus frequency) and Fig. 6(b) (output voltage versus duty cycle) show the output voltage at the beginning of the pulse, with an input voltage of $V_{\text{DL}} = 400$ V (blue lines) and at the end of the pulse discharged to an input voltage of $V_{\text{DL}} = 330$ V (red lines). The solid lines are the nominal transfer characteristics and the dashed lines represent the component tolerances. If the modulator is operated with a constant frequency f_A, the output voltage starting in point A ($V_{\text{out}} = 12.75$ kV) is decreasing and will end in point E ($V_{\text{out}} = 10.6$ kV) [see Fig. 6(a) and (b)]. The crosses depicted in Fig. 6(b), marked with D_{fA}, D'_{fA}, and D''_{fA}, define the minimum duty cycles, which allow zero voltage switching (ZVS) if the SPRC-Bm is operated above the resonance frequency [see Fig. 6(a)]. To compensate the voltage droop, the frequency f_A is reduced during the pulse until it reaches f_B in point B, see Fig. 6(a). The compensation is realized by decreasing the frequency linearly, if the output voltage V_{out} crosses a certain limit. The reduction of the frequency leads to an overlap of the output voltage characteristics [compare Fig. 6(b) and (c)], but the minimum duty cycles D_{fA}, D'_{fA}, and D''_{fA} are moving toward higher duty cycle values and ending in D_{fB}, D'_{fB}, and D''_{fB}. This leads to a reduced ZVS range, which has to be considered during the design process. The minimum duty cycles can be calculated by

$$D = \left(\frac{\pi}{2} - \varphi_{\text{ZVS}}\right)\frac{2}{\pi}, \quad \text{with} \quad \varphi_{\text{ZVS}} = \varphi - \varphi_{Tot}. \tag{11}$$

The angle φ is the input impedance angle between the first harmonic of the full bridge output voltage $V_{\text{AB}(1)}$ and the resonant current $I_{\text{LS}(1)}$ [see Fig. 7(a)] and is calculated with (35) in [5]. This angle has to be reduced by the interlocking angle φ_{Tot} to ensure ZVS in all switches of the SPRC Bm. Fig. 7(b) shows the ZVS violation where the interlocking angle is not considered in the switching signals.

2) Component Tolerances: The tolerance discussion is based on the converter design given in [22], which is the prototype system related to the proposed controller design. The total tolerance $s(k)$ of parts that are formed by k components is given by

$$s(k) = \frac{s_1}{\sqrt{k}} \tag{12}$$

where s_1 is the tolerance of a single component. The tolerance s_1 of the used NP0 ceramic capacitors in [22] is 5%. This results in a total tolerance $s_{CS}(k) = \pm 0.167\%$ for C_{S} which is made of 896 capacitors and a total tolerance $s_{CP}(k) = \pm 0.34\%$ for C_{P} which is made of 216 NP0 capacitors. Therefore, it can be concluded that the resonant capacitors have a negligible tolerance. However, the inductor L_{S} that is a single component has a relatively large tolerance. The influence of this tolerance

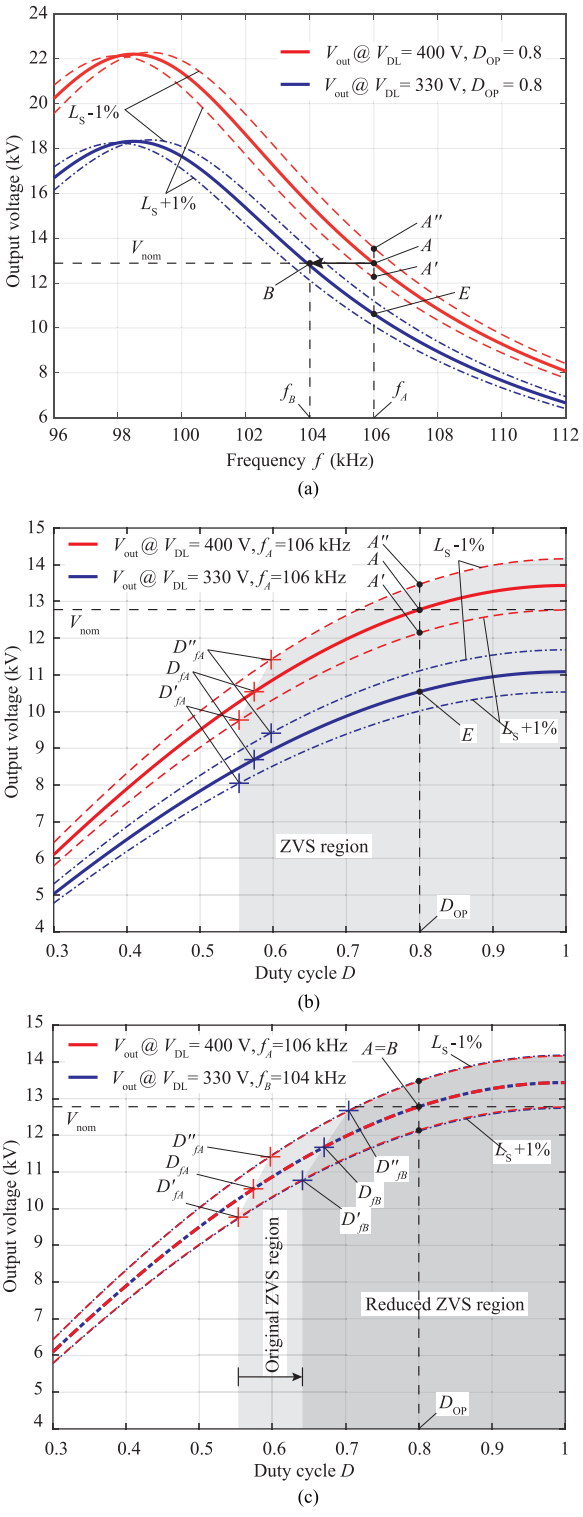

Fig. 6. Output voltage characteristics given for different input voltages in (a) versus frequency and in (b) and (c) versus duty cycle. The red curves are the voltages at the beginning of the pulse with an input voltage $V_{\mathrm{DL}} = 400$ V and the blue curves are the voltages at the end of the pulse with $V_{\mathrm{DL}} = 330$ V due to the voltage drop of the main capacitor. The dashed lines indicate the tolerances of the series inductance L_{S}. If the modulator would be operated with constant frequency f_A, the output voltage starting in point A is decreasing and will end in point E [(a) and (b)]. To compensate the voltage droop, the frequency f_A is reduced until it reaches f_B in point B [(a) and (c)]. The reduction of the frequency leads to an overlap of the output voltage characteristics and a constant output voltage, respectively, but also to a reduction of the ZVS range (c).

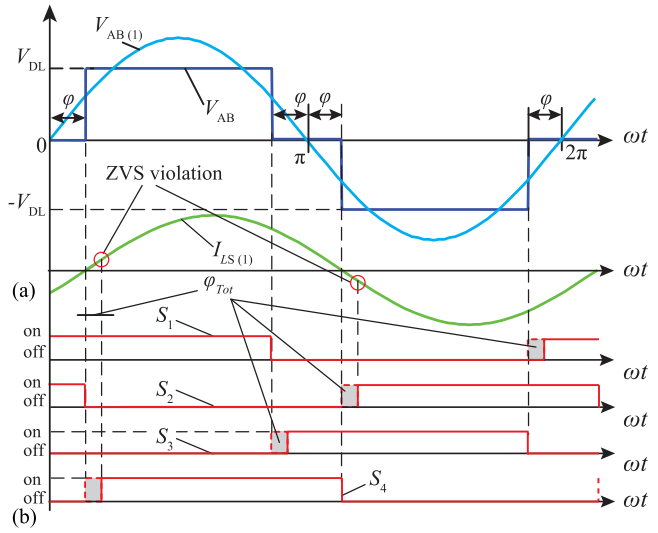

Fig. 7. (a) Input impedance angle φ between $V_{\mathrm{AB}(1)}$ and $I_{L\mathrm{S}\,(1)}$. (b) Switching signals of the switches $S_1 - S_4$ with the interlocking angle φ_{Tot}. A ZVS violation occurs in the switches S_2 and S_4 of the SPRC-Bm because the current $I_{L\mathrm{S}\,(1)}$ crosses zero before the switches S_2 and S_4 turn on.

is clearly visible in Fig. 6. The variation of the inductance by $\pm 1\%$ (dashed lines) results in a voltage change of $\mp 5\%$ in point A' and A'' compared to the nominal value V_{nom} (solid lines) in point A.

B. Input and Output Voltage Balancing

For IPOS systems equal power sharing is achieved by ensuring OVS that results in equal input current sharing (ICS) [12]. Unfortunately, the ICS of the IPOS system does not lead to equal IVS of the SPRC-Bms of the embedded ISOP systems. Due to the tolerances of the resonant inductor each of the two SPRC-Bms in the ISOP system could transfer different amounts of power to the output, which is provided by their input capacitors. This results in an input voltage divergence that has to be compensated either with the help of an auxiliary circuit or by control.

If the input voltage balancing cannot be achieved by control, since for example the ZVS condition is violated, different auxiliary circuits can be used to balance the input voltage. The input voltage balancing concept realized with an auxiliary circuit and an output voltage balancing by control is given first. Afterward, additionally a method based on an input and output voltage balancing purely by control is presented.

1) Input Voltage Balancing by Auxiliary Circuit and Output Voltage Balancing by Control: In Fig. 8(a), the input voltage balancing is achieved with switched auxiliary resistors that are in parallel to the dc-link capacitors C_{DL} [23]. The resistors discharge the input capacitors to equal voltages by turning on their switches, hence leading to an equal power sharing. However, the unbalanced power has to be dissipated by the auxiliary resistors. This drawback is avoided by the circuit shown in Fig. 8(b) [24]. There, the unbalanced power from one capacitor is used to charge the other capacitor until both have equal voltages. Therefore, the active buck balancing circuit is used for the input

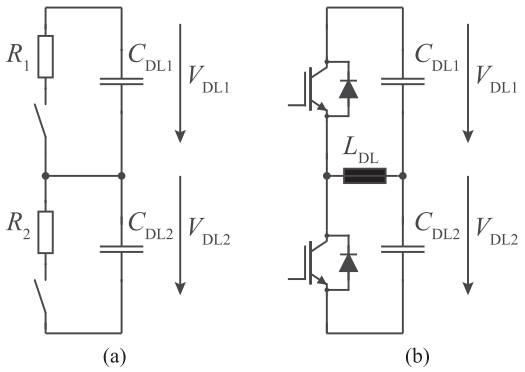

Fig. 8. (a) Switched resistor balancing and (b) active balancing.

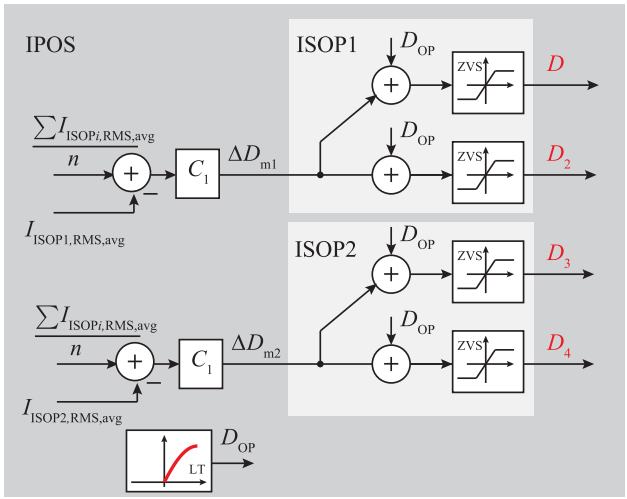

Fig. 9. Control block diagram of the output voltage balancing, based on the resonant currents where n is the number of ISOP systems. The operation point duty cycle D_{OP} is given from a lookup table (LT).

voltage balancing. If $V_{\mathrm{DL1}} > V_{\mathrm{DL2}}$, the circuit acts as a buck converter where V_{DL1} is the input voltage and V_{DL2} is the output voltage. If $V_{\mathrm{DL1}} < V_{\mathrm{DL2}}$, the circuit acts as a buck converter where V_{DL2} is the input voltage and V_{DL1} is the output voltage.

For the output voltage balancing, the concept shown in Fig. 9 could be employed. If it is not possible to access all output voltages, e.g. the high-voltage transformers are oil isolated, an alternative way to balance the output voltages of each ISOP system is to balance the resonant currents of each ISOP system. A comparison of the dynamic behavior between the averaged output voltages ($V_{\mathrm{O1,avg}}$, $V_{\mathrm{O2,avg}}$) and the averaged resonant RMS currents ($I_{\mathrm{ISOP1,RMS,avg}}$, $I_{\mathrm{ISOP2,RMS,avg}}$) of the ISOP systems is shown in Fig. 10. There

$$I_{\mathrm{ISOP1,RMS,avg}} = \frac{I_{\mathrm{res1,RMS}} + I_{\mathrm{res2,RMS}}}{2} \tag{13}$$

and

$$I_{\mathrm{ISOP2,RMS,avg}} = \frac{I_{\mathrm{res3,RMS}} + I_{\mathrm{res4,RMS}}}{2} \tag{14}$$

where $I_{\mathrm{res},i,\mathrm{RMS}}$ is the resonant rms current of the ith SPRC-Bm [see Fig. 4(a)].

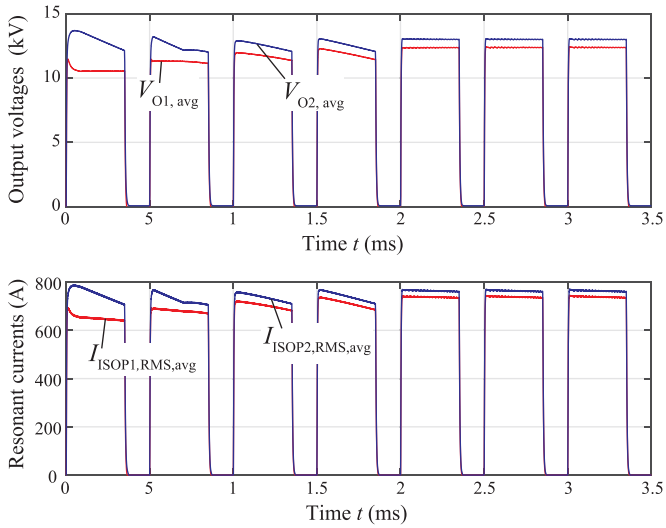

Fig. 10. Comparison of the dynamic behavior between the averaged output voltages ($V_{\mathrm{O1,avg}}, V_{\mathrm{O2,avg}}$) and the averaged resonant RMS currents ($I_{\mathrm{ISOP1,RMS,avg}}, I_{\mathrm{ISOP2,RMS,avg}}$) of the ISOP systems.

In order that the duty cycle variation $\Delta D_{\mathrm{m}i}$ in the IPOS control loop does not interfere with the operating point duty cycle D_{OP}, the decoupling condition

$$\sum \Delta D_{\mathrm{m}i} = 0 \tag{15}$$

has to be fulfilled. The proof that $\Delta D_{\mathrm{m}i}$ is not interfering with D_{OP} is (for $n = 2$)

$$\begin{aligned} \Delta D_{m1} &= \left(\frac{\sum \Delta I_{\mathrm{ISOP}i,\mathrm{RMS,avg}}}{n} - \Delta I_{\mathrm{ISOP1,RMS,avg}} \right) C_1 \\ \Delta D_{m2} &= \left(\frac{\sum \Delta I_{\mathrm{ISOP}i,\mathrm{RMS,avg}}}{n} - \Delta I_{\mathrm{ISOP2,RMS,avg}} \right) C_1 \\ \Delta D_{m1} &+ \Delta D_{m2} = 0 \end{aligned} \tag{16}$$

with

$$\Delta I_{\mathrm{ISOP2,RMS,avg}} = \sum \Delta I_{\mathrm{ISOP}i,\mathrm{RMS,avg}} - \Delta I_{\mathrm{ISOP1,RMS,avg}}. \tag{17}$$

The small signal control block diagram and the open-loop bode diagram of the output voltage compensation, with (dashed lines) and without (solid lines) compensator, are shown in Fig. 11. The compensator $C_1(s)$ is a pure integral controller with $T_I = 0.5$, leading to the phase margins of $\mathrm{PM}_{fB} = 53.6°$ and $\mathrm{PM}_{fA} = 83.2°$

$$C_1(s) = \frac{1}{sT_I}. \tag{18}$$

The gain margins are $\mathrm{GM}_{fB} = 62.7$ dB and $\mathrm{GM}_{fA} = 65.6$ dB, with $f_B = 104$ kHz and $f_A = 106$ kHz, defining the frequency range of the droop compensation. The minor influence of f_A and f_B on the transfer characteristics is shown in Fig. 11. Since the droop compensation reduces the influence of the variable input voltage, the duty cycle to the averaged resonant RMS current transfer function is derived from the small signal control block diagram of the reduced IPOS system with fix input voltage

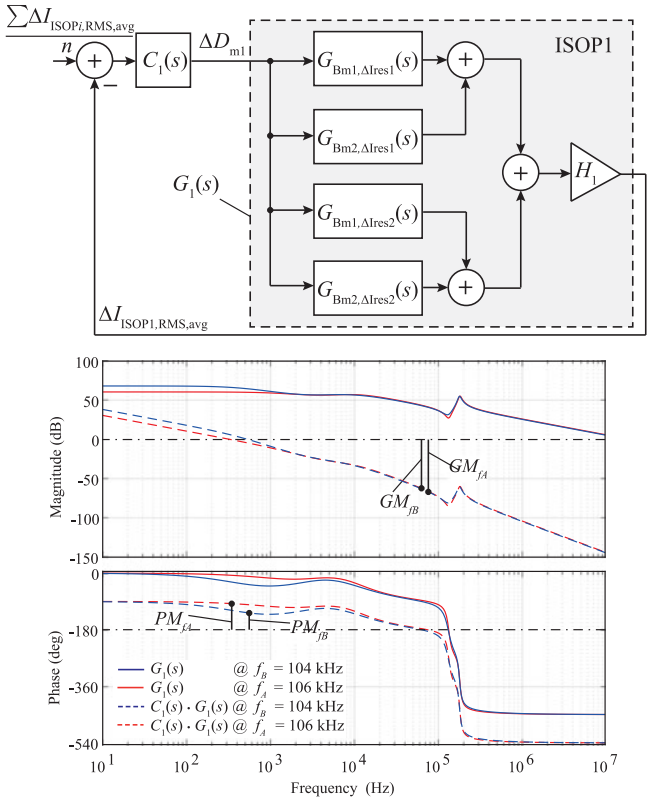

Fig. 11. Small signal control block diagram and open-loop bode diagram of the output voltage compensation based on the resonant currents of an ISOP system, with (dashed lines) and without (solid lines) compensator. The compensator $C_1(s)$ is a pure integral controller with $T_I = 0.5$ leading to the phase margins of $PM_{fB} = 53.6°$ and $PM_{fA} = 83.2°$. The gain margins are $GM_{fB} = 62.7$ dB and $GM_{fA} = 65.6$ dB.

shown in Fig. 11 as

$$G_1(s) = \frac{\Delta I_{\text{ISOPi,RMS,avg}}}{\Delta D_{\text{m}i}} = [G_{\text{Bm1,}\Delta\text{Ires1}}(s) + G_{\text{Bm2,}\Delta\text{Ires1}}(s) + G_{\text{Bm1,}\Delta\text{Ires2}}(s) + G_{\text{Bm2,}\Delta\text{Ires2}}(s)] \cdot H_1. \quad (19)$$

$G_{\text{Bm}i,\Delta\text{Ires}j}(s)$ is the resonant rms current transfer function from the ith SPRC-Bm to the jth resonant RMS current and the constant factor $H_1 = 0.5$ to calculate the average.

A detailed derivation of the transfer function $G_1(s)$ is given in Appendix B.

2) Input and Output Voltage Balancing by Control: The control strategy for the ISOP system as depicted in Fig. 12 is discussed in a first step and afterward the strategy for the IPOS system based on the regulation of the output voltages is developed. In the literature, several possibilities to control ISOP systems exist. The concepts presented in [11]–[13] show an easily implementable control strategy that employs just two control loops. In the considered system, these two loops are further reduced to one, because D_{OP}, which is responsible for the operation point is given from a lookup table (LT) (see Fig. 12). To ensure an equal power sharing of the ISOP system one has to ensure an equal IVS that automatically results in equal output current sharing and respectively equal power sharing [12]. For IPOS systems, equal power sharing is achieved by ensuring OVS that leads to

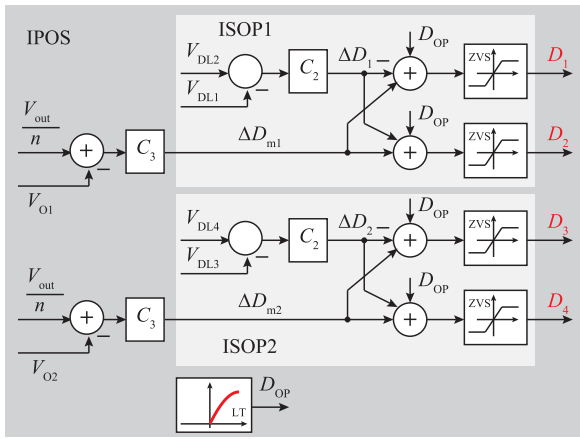

Fig. 12. Control block diagram of the input and output voltage balancing, where n is the number of ISOP systems. The operation point duty cycle D_{OP} is given from a lookup table (LT).

equal ICS [12]. In order that both the duty cycle variation ΔD_i in the ISOP and $\Delta D_{\text{m}i}$ in the IPOS control loop do not interfere with the operation point duty cycle D_{OP}, the decoupling conditions

$$\sum \Delta D_i = 0 \quad \text{and} \quad \sum \Delta D_{\text{m}i} = 0 \quad (20)$$

have to be fulfilled. The proof from (16) for $\Delta D_{\text{m}i}$ is still valid by replacing the resonant currents from Fig. 9 by the output voltages shown in Fig. 12. The decoupling condition for ΔD_i is fulfilled by applying the same value ΔD_i for each SPRC-Bm with opposite sign within an ISOP system. The small signal control block diagrams and open-loop bode diagrams of the input voltage and the output voltage compensation, with (dashed lines) and without (solid lines) compensators, are shown in Fig. 13(a) and (b), respectively. The compensators $C_2(s)$ and $C_3(s)$ are simple proportional controllers with $K_{p2} = 0.025$ and $K_{p3} = 152.368\text{E}-6$, resulting in a phase margins of $PM_1 = 91°$ and $PM_2 = 75°$. The gain margins are $GM_1 = 62$ dB and $GM_2 = 19.5$ dB. Again, both open-loop functions are evaluated for different switching frequencies ($f_B = 104$ kHz, $f_A = 106$ kHz) to point out their minor influences on the transfer characteristics [see Fig. 13(a) and (b)], hence leading to fix compensator gains for the full droop compensation frequency range.

Using the transfer functions from the small signal model of the reduced IPOS system with variable input voltage and the control loop depicted in Fig. 13(a), the duty cycle to input voltage difference transfer function can be obtained as

$$G_2(s) = \frac{\Delta V_{\text{DL2}} m \Delta V_{\text{DL1}}}{\Delta D_1} = -G_{\text{Bm1,}\Delta\text{VDL1}}(s) + G_{\text{Bm2,}\Delta\text{VDL1}}(s) + G_{\text{Bm1,}\Delta\text{VDL2}}(s) - G_{\text{Bm2,}\Delta\text{VDL2}}(s) \quad (21)$$

where $G_{\text{Bm}i,\Delta\text{VDL}j}$ is the input voltage transfer function from the ith SPRC-Bm to the jth input voltage. Due to the droop compensation the duty cycle to output voltage transfer function is derived from the small signal model of the reduced ISOP-IPOS system with fix input voltage and the control loop depicted

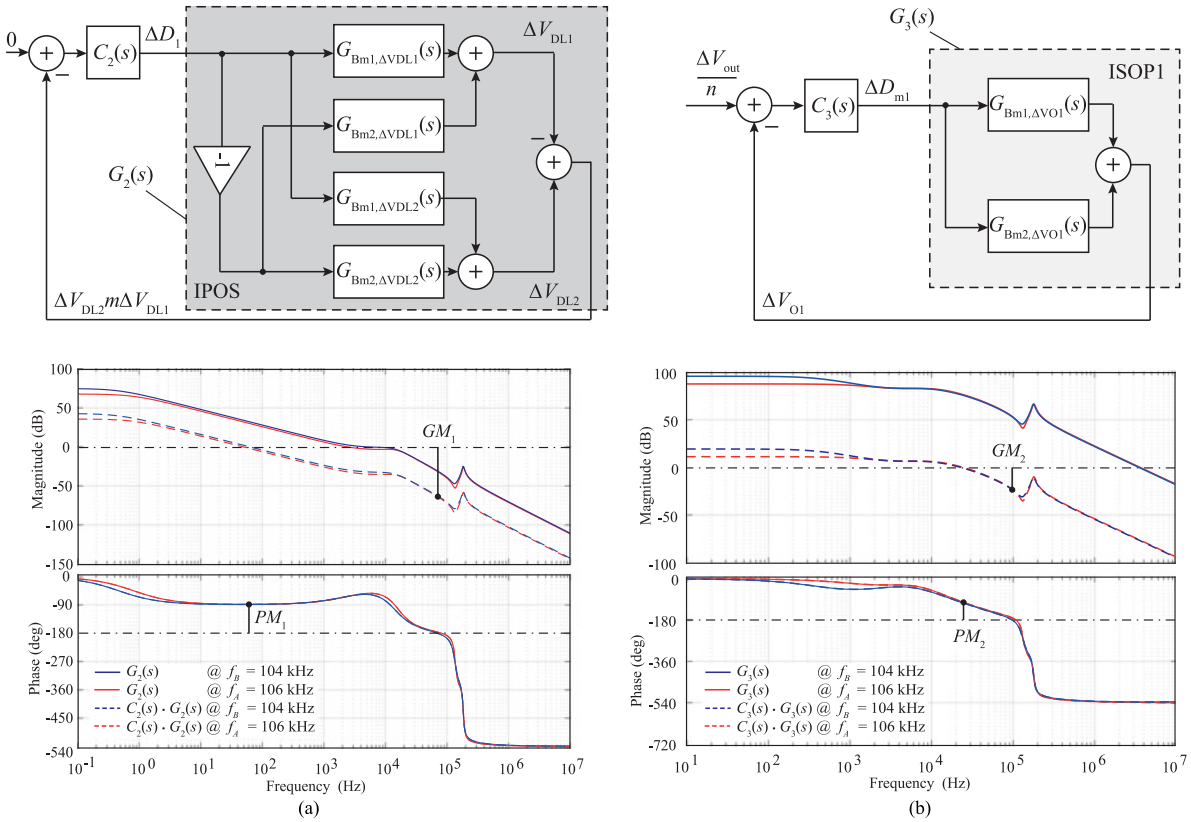

Fig. 13. Small signal control block diagram and open-loop bode diagram of (a) the input voltage regulation and (b) the output voltage compensation with (dashed lines) and without (solid lines) compensator. The compensators $C_2(s)$ and $C_3(s)$ are proportional controllers with $K_{p2} = 0.025$ and $K_{p3} = 152.368\text{E}{-6}$ leading to the phase margins of $\text{PM}_1 = 91°$ and $\text{PM}_2 = 75°$. The gain margins are $\text{GM}_1 = 62$ dB and $\text{GM}_2 = 19.5$ dB. Both diagrams are given for the frequency range of the droop compensation to point out their minor influences on the transfer characteristics.

in Fig. 13(b) as

$$G_3(s) = \frac{\Delta V_{O1}}{\Delta D_{m1}} = G_{\text{Bm1},\Delta\text{VO1}}(s) + G_{\text{Bm2},\Delta\text{VO1}}(s) \qquad (22)$$

where $G_{\text{Bm}i,\Delta\text{VO1}}$ is the output voltage transfer function from the ith SPRC-Bm to the first output voltage.

A detailed derivation of the transfer functions $G_2(s)$ and $G_3(s)$ is given in Appendix B.

IV. Measurement and Simulation Results

In the following, first measurement results of the IPOS system [see Fig. 4(a)] utilizing the input voltage balancing by an auxiliary circuit and the output voltage balancing by control are presented. Afterward, simulation results based on the input and the output voltage balancing by control only are shown.

A. Measurement Results of the IPOS System Based on the Input Voltage Balancing by an Auxiliary Circuit and Output Voltage Balancing by Control

The measured averaged resonant RMS currents $I_{\text{ISOP1,RMS,avg}}$, $I_{\text{ISOP2,RMS,avg}}$ and the measured ISOP output voltages (V_{O1}, V_{O2}, and V_{out}) for a system without output voltage balancing are depicted in Fig. 14(a) and (b). For compensating the droop the switching frequency is decreased from 107 to 104.8 kHz [see Fig. 14(c)]. The measured resonance inductance (L_S), the input voltages (V_DL), and the load resistor (R_L) are given in Table III. The IPOS system is operated with an output voltage of 23 kV compared to the nominal output voltage of 25.5 kV, due to the component tolerances and the different load value (compare nominal load value in Table IV). Fig. 15 shows all voltages and currents in case of an active output voltage balancing. The droop compensation by adapting the switching frequency is the same as depicted in Fig. 14(c). The applied pure integral compensator value is $T_I = 0.5$ and the control cycle of the implemented control algorithm is 80 kS/s. The output voltages are well balanced that leads to an equally distributed power stress between the single SPRC-Bms. Fig. 16 shows the components of a single SPRC-Bm consisting of a full-bridge with six MOSFETs in parallel for each switch, a series inductor L_S, a series capacitor C_S [see Fig. 16(a)], the high-voltage high-frequency transformer [see Fig. 16(b)] and an output rectifier with parallel capacitor C_P [see Fig. 16(c)]. The active input voltage balancing auxiliary circuit [see Fig. 8(b)], is shown in Fig. 16(d). Two of these auxiliary circuits are used for the reduced IPOS prototype system.

B. Simulation Results of the IPOS System Based on the Input and Output Voltage Balancing by Control

The pure control based approach is more sensitive to the ZVS reduction due to the input voltage droop and the component tolerances (see Section III-A1). This can result in destructive hard switching of the full bridge switches. In order to obtain

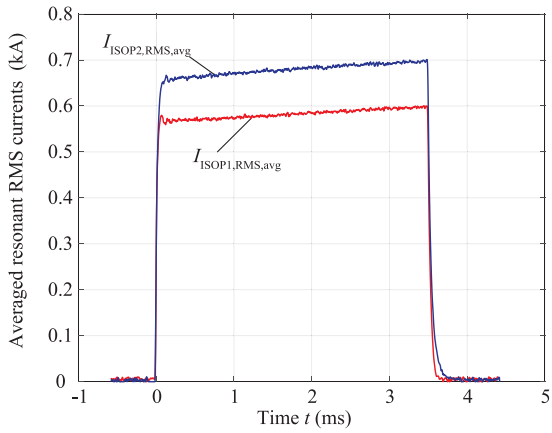

(a)

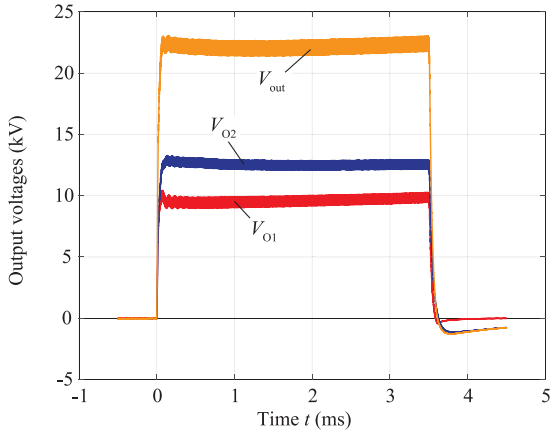

(b)

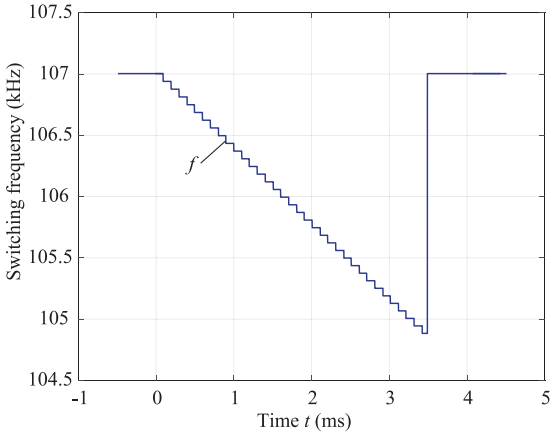

(c)

Fig. 14. Measured IPOS signals with no output voltage balancing. (a) Averaged resonant RMS currents $I_{\text{ISOP1,RMS,avg}}$, $I_{\text{ISOP2,RMS,avg}}$. (b) Output voltages V_{O1}, V_{O2}, and V_{out}. (c) Adaption of the switching frequency for the droop compensation with a start frequency of 107 kHz and an end frequency of 104.8 kHz.

TABLE III
MEASURED COMPONENT AND INITIAL VALUES

	Bm1	Bm2	Bm3	Bm4
L_{S} (μH)	4.4	4.31	4.25	4.29
V_{DL} (V)	400.8	400.2	399.3	401.7
R_{L} (Ω)	1220			

TABLE IV
NOMINAL COMPONENT VALUES WITH TOLERANCES AND INITIAL VALUES USED FOR THE SIMULATIONS

	Bm1	Bm2	Bm3	Bm4
L_{S} (μH)	4.241	4.199	4.157	4.199
C_{S} (nF)	840	840	840	840
C_{P} (nF)	4.234	4.234	4.234	4.234
$\ddot{u}$ ($-$)	20	20	20	20
C_{DL} (mF)	30	31.5	31.5	30
V_{DL} (V)	409.75	390.25	390.25	409.75
C_{f} (nF)	20		20	
R_{L} (Ω)	1150			

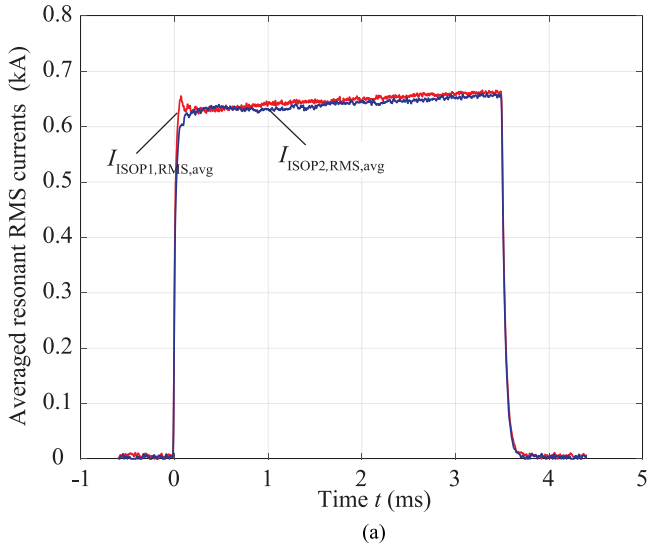

(a)

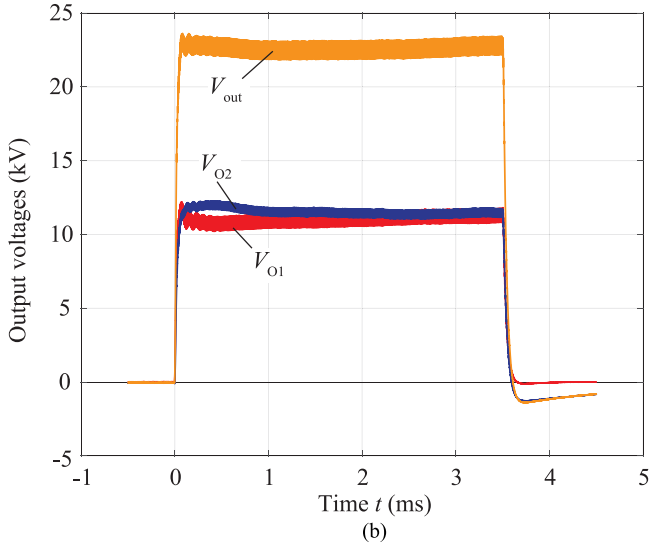

(b)

Fig. 15. Measured IPOS signals with active output voltage balancing. (a) Averaged resonant RMS currents $I_{\text{ISOP1,RMS,avg}}$, $I_{\text{ISOP2,RMS,avg}}$. (b) Output voltages V_{O1}, V_{O2}, and V_{out}. The adaption of the switching frequency for the droop compensation with a start frequency of 107 kHz and an end frequency of 104.8 kHz is the same as depicted in Fig. 14(c). The used integral compensator value is $T_{\text{I}} = 0.5$.

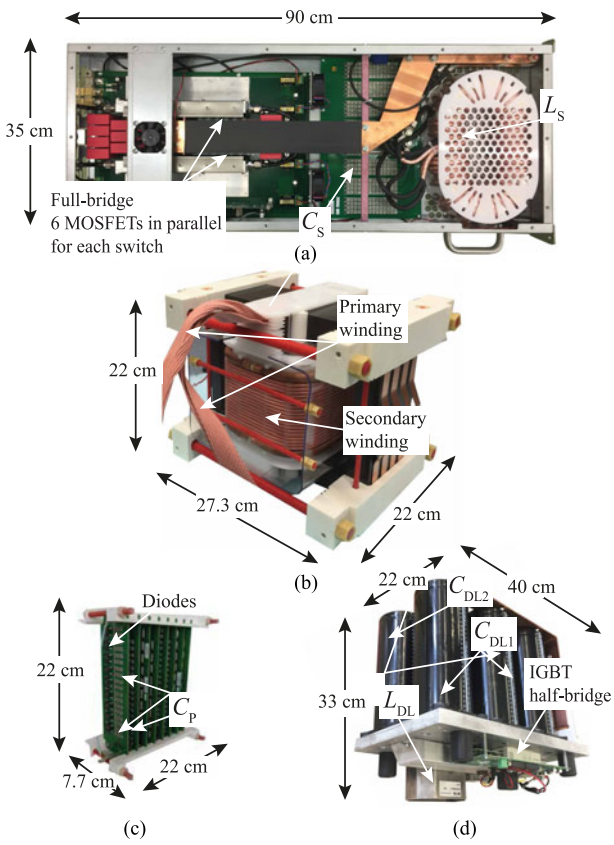

Fig. 16. Single SPRC-Bm consisting of (a) a full-bridge with six MOSFETs in parallel for each switch, a series inductor L_S and a series capacitor C_S, (b) an high-voltage high-frequency transformer, and (c) an output rectifier with parallel capacitor C_P. (d) Auxiliary circuit for the input voltage balancing [see Fig. 8(b)].

a robust system, the solution with auxiliary circuit was implemented and the pure control based is, therefore, verified only by simulations.

Fig. 17(a) and (b) show the input and output voltages in case the modules have nominal component values plus tolerances. The inductance values are varied by $\pm 1\%$ and the dc-link capacitance values by 5% with according initial voltages. The exact values are given in Table IV. All modules are operated interleaved with a start switching frequency of 106 kHz, an end frequency of 104.9 kHz [see Fig. 17(c)] and a duty cycle D_{OP} of 0.8. This results in an output voltage operating point of 25.5 kV ($=2 \times 12.75$ kV). The pulse repetition rate is increased to 200 Hz to decrease the simulation times and memory consumption. In the pulse break after each 3.5 ms pulse, the dc-link capacitors are recharged to 800 V in total.

Applying the control loops given in Section III-B2 results in a stable operation as can be seen in Fig. 17(a) and 17(b). The input voltage controller compensates the voltage difference after four pulses. During these four pulses, the droop compensation is not active because the output voltage does not reach the nominal voltage limit so that the modules are operated with constant frequency. The output voltage compensation is also achieved after four pulses. The used compensator values are $K_{p2} = 0.025$ and $K_{p3} = 152.368E{-}6$.

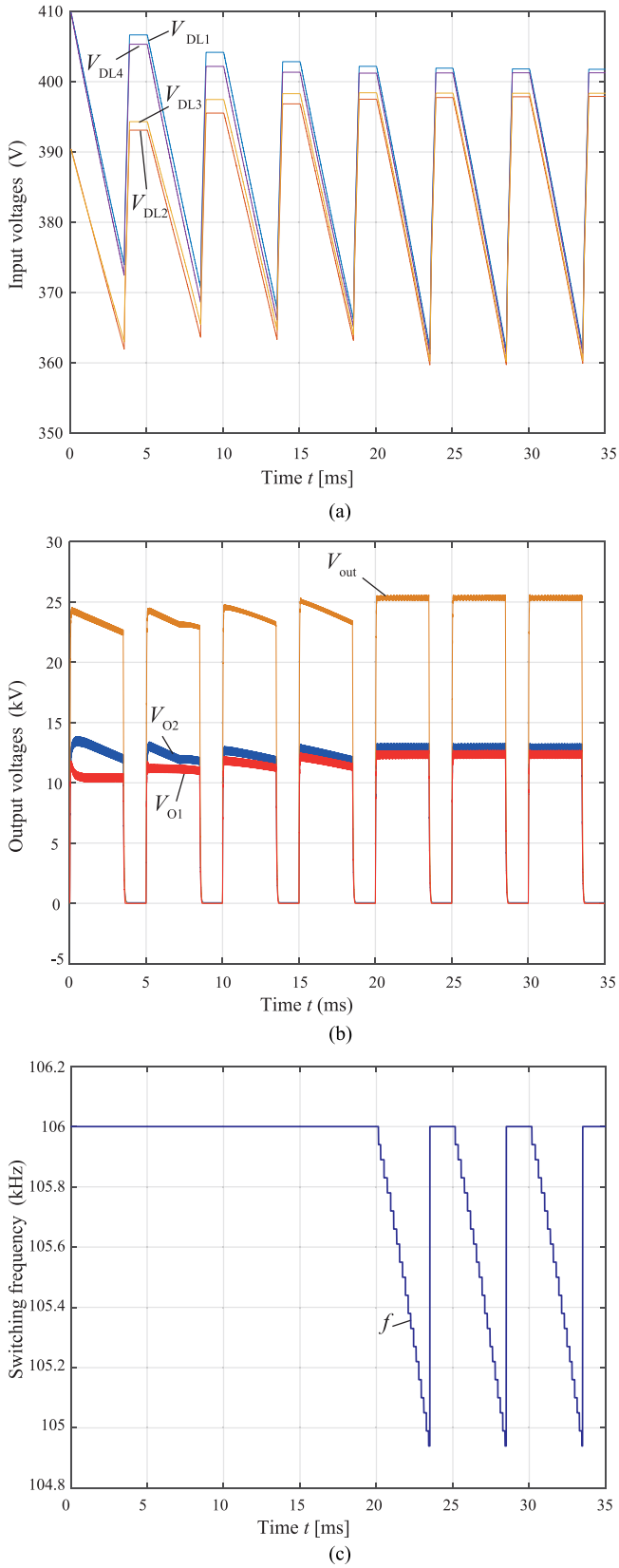

Fig. 17. (a) Input voltages $V_{DL1}, V_{DL2}, V_{DL3}$, and V_{DL4}, in case all control loops are active. (b) Output voltages V_{O1}, V_{O2}, and V_{out}. (c) Adaption of the switching frequency for the droop compensation with a start frequency of 106 kHz and an end frequency of 104.9 kHz. The compensator values are $K_{p2} = 0.025$ and $K_{p3} = 152.368\text{E}{-}6$.

V. Conclusion

In this paper, a large signal model for a nested ISOP-IPOS system with non constant input voltages is presented in detail. Additionally, the transition to the small signal model is derived. Two control strategies for an optimal power sharing, input and output voltage balancing are given for the nested system. In the first case, the input voltage balancing is achieved with the help of an auxiliary circuit and the output voltage balancing by control of the resonant currents. The performance of the proposed controller is demonstrated with measurement results. Furthermore an input and output voltage balancing by control is presented and verified by simulations. In addition, the effects of the output voltage droop compensation of the IPOS system depending on the dc-link capacitor and resonant tank components tolerances is shown.

Appendix A

The full set of equations of the reduced IPOS system consisting of four SPRC-Bm with variable input voltage is given below. Each set (25), (26), (27), (28) is for a single SPRC-Bm. Equations (23) and (24) are the linking equations for the parallel output connection of the ISOP system and the series output connection of the IPOS system. Equations (25e), (26e), (27e), and (28e) consider the variable input voltage of each SPRC-Bm. All equations are related to Fig. 4(b) and all magnitudes and components are transferred to the primary sides of the transformers with $R'_{\mathrm{L}} = R_{\mathrm{L}}/\ddot{u}^2$, $C'_{\mathrm{f}x} = C_{\mathrm{f}x}\ddot{u}^2$, and $C'_{\mathrm{P}x} = C_{\mathrm{P}x}\ddot{u}^2$. If a system with constant input voltage is investigated x_{10}, x_{11}, x_{21}, and x_{22} have to be replaced by V_{DL0}, V_{DL02}, V_{DL03}, and V_{DL04} and (25e), (26e), (27e), and (28e) are removed from the system

$$\begin{aligned}\dot{x_5} =& -\frac{x_5 + x_{16}}{C'_{\mathrm{f}} R'_{\mathrm{L}}} + \frac{2\sqrt{x_1^2 + x_2^2}}{C'_{\mathrm{f}}\pi}[1 + \cos(\psi)] \\ &+ \frac{2\sqrt{x_6^2 + x_7^2}}{C'_{\mathrm{f}}\pi}[1 + \cos(\psi_2)] \end{aligned} \tag{23}$$

$$\begin{aligned}\dot{x_{16}} =& -\frac{x_{16} + x_5}{C'_{\mathrm{f2}} R'_{\mathrm{L}}} + \frac{2\sqrt{x_{12}^2 + x_{13}^2}}{C'_{\mathrm{f2}}\pi}[1 + \cos(\psi_3)] \\ &+ \frac{2\sqrt{x_{17}^2 + x_{18}^2}}{C'_{\mathrm{f2}}\pi}[1 + \cos(\psi_4)] \end{aligned} \tag{24}$$

$$\dot{x_1} = \frac{x_{10}\sin(D\pi)}{\pi L_{\mathrm{S}}} - \frac{r x_1 + x_3 + x_a}{L_{\mathrm{S}}} + \omega x_2 \tag{25a}$$

$$\dot{x_2} = \frac{x_{10}[\cos(D\pi) - 1]}{\pi L_{\mathrm{S}}} - \frac{r x_2 + x_4 + x_b}{L_{\mathrm{S}}} - \omega x_1 \tag{25b}$$

$$\dot{x_3} = \frac{1}{C_{\mathrm{S}}} x_1 + \omega x_4 \tag{25c}$$

$$\dot{x_4} = \frac{1}{C_{\mathrm{S}}} x_2 - \omega x_3 \tag{25d}$$

$$\dot{x_{10}} = -\frac{(4\sqrt{x_1^2 + x_2^2} - 2x_5 C'_{\mathrm{p}}\omega)}{\pi} \frac{x_5}{x_{10}} \frac{1}{C_{\mathrm{DL1}}} \tag{25e}$$

$$x_a = \frac{1}{\pi C'_{\mathrm{p}}\omega}(x_1 \sin(\psi)^2 + x_2\mu) \tag{25f}$$

$$x_b = \frac{1}{\pi C'_{\mathrm{p}}\omega}(x_2 \sin(\psi)^2 - x_1\mu) \tag{25g}$$

$$\cos\psi = 1 - \frac{x_5 C'_{\mathrm{p}}\omega}{\sqrt{x_1^2 + x_2^2}} \tag{25h}$$

$$\mu = \psi - \sin(\psi)\cos(\psi) \tag{25i}$$

$$\dot{x_6} = \frac{x_{11}\sin(D_2\pi)}{\pi L_{\mathrm{S2}}} - \frac{r x_6 + x_8 + x_{a2}}{L_{\mathrm{S2}}} + \omega x_7 \tag{26a}$$

$$\dot{x_7} = \frac{x_{11}[\cos(D_2\pi) - 1]}{\pi L_{\mathrm{S2}}} - \frac{r x_7 + x_9 + x_{b2}}{L_{\mathrm{S2}}} - \omega x_6 \tag{26b}$$

$$\dot{x_8} = \frac{1}{C_{\mathrm{S2}}} x_6 + \omega x_9 \tag{26c}$$

$$\dot{x_9} = \frac{1}{C_{\mathrm{S2}}} x_7 - \omega x_8 \tag{26d}$$

$$\dot{x_{11}} = -\frac{(4\sqrt{x_6^2 + x_7^2} - 2x_5 C'_{\mathrm{P2}}\omega)}{\pi} \frac{x_5}{x_{11}} \frac{1}{C_{\mathrm{DL2}}} \tag{26e}$$

$$x_{a2} = \frac{1}{\pi C'_{\mathrm{P2}}\omega}(x_6 \sin(\psi_2)^2 + x_7\mu_2) \tag{26f}$$

$$x_{b2} = \frac{1}{\pi C'_{\mathrm{P2}}\omega}(x_7 \sin(\psi_2)^2 - x_6\mu_2) \tag{26g}$$

$$\cos\psi_2 = 1 - \frac{x_5 C'_{P2}\omega}{\sqrt{x_6^2 + x_7^2}} \tag{26h}$$

$$\mu_2 = \psi_2 - \sin_2(\psi_2)\cos(\psi_2) \tag{26i}$$

$$\dot{x_{12}} = \frac{x_{21}\sin(D_3\pi)}{\pi L_{\mathrm{S3}}} - \frac{r x_{12} + x_{14} + x_{\mathrm{a3}}}{L_{\mathrm{S3}}} + \omega x_{13} \tag{27a}$$

$$\dot{x_{13}} = \frac{x_{21}[\cos(D_3\pi) - 1]}{\pi L_{\mathrm{S3}}} - \frac{r x_{13} + x_{15} + x_{\mathrm{b3}}}{L_{\mathrm{S3}}} - \omega x_{12} \tag{27b}$$

$$\dot{x_{14}} = \frac{1}{C_{\mathrm{S3}}} x_{12} + \omega x_{15} \tag{27c}$$

$$\dot{x_{15}} = \frac{1}{C_{\mathrm{S3}}} x_{13} - \omega x_{14} \tag{27d}$$

$$\dot{x_{21}} = -\frac{(4\sqrt{x_{12}^2 + x_{13}^2} - 2x_{16} C'_{\mathrm{P3}}\omega)}{\pi} \frac{x_{16}}{x_{21}} \frac{1}{C_{\mathrm{DL3}}} \tag{27e}$$

$$x_{a3} = \frac{1}{\pi C'_{\mathrm{P3}}\omega}(x_{12} \sin(\psi_3)^2 + x_{13}\mu_3) \tag{27f}$$

$$x_{b3} = \frac{1}{\pi C'_{\mathrm{P3}}\omega}(x_{13} \sin(\psi_3)^2 - x_{12}\mu_3) \tag{27g}$$

$$\cos\psi_3 = 1 - \frac{x_{16} C'_{\mathrm{P3}}\omega}{\sqrt{x_{12}^2 + x_{13}^2}} \tag{27h}$$

$$\mu_3 = \psi_3 - \sin(\psi_3)\cos(\psi_3) \tag{27i}$$

$$\dot{x_{17}} = \frac{x_{22}\sin(D_4\pi)}{\pi L_{\mathrm{S4}}} - \frac{r x_{17} + x_{19} + x_{\mathrm{a4}}}{L_{\mathrm{S4}}} + \omega x_{18} \tag{28a}$$

$$\dot{x_{18}} = \frac{x_{22}[\cos(D_4\pi) - 1]}{\pi L_{\mathrm{S4}}} - \frac{r x_{18} + x_{20} + x_{\mathrm{b4}}}{L_{\mathrm{S4}}} - \omega x_{17} \tag{28b}$$

$$\dot{x_{19}} = \frac{1}{C_{\mathrm{S4}}} x_{17} + \omega x_{20} \tag{28c}$$

$$\dot{x_{20}} = \frac{1}{C_{\mathrm{S4}}} x_{18} - \omega x_{19} \tag{28d}$$

TABLE V
COMPONENT VALUES AND OPERATION POINTS OF THE SPRC BMS OF AN IPOS SYSTEM WITH FIXED AND VARIABLE INPUT VOLTAGE, USED FOR THE LINEARIZATION

Bm1	Bm2	Bm3	Bm4		
Component and operation point input values					
L_{S}	L_{S2}	L_{S3}	L_{S4}	(μH)	4.199
C_{S}	C_{S2}	C_{S3}	C_{S4}	(nF)	840
C'_{P}	C'_{P2}	C'_{P3}	C'_{P4}	(μF)	1.696
r	r	r	r	(Ω)	0.01
C'_{f}		C'_{f2}		(μF)	8
R'_{L}				(Ω)	2.875
C_{DL1}	C_{DL2}	C_{DL3}	C_{DL4}	(mF)	30
ω_0	ω_{02}	ω_{03}	ω_{04}	(krad/s)	$2\cdot\pi\cdot106$
D_0	D_{02}	D_{03}	D_{04}	($-$)	0.8
Operation point magnitudes of a system with fixed input voltage					
V_{DL0}	V_{DL02}	V_{DL03}	V_{DL04}	(V)	400
x_{01}	x_{06}	x_{012}	x_{017}	(A)	-324.11
x_{02}	x_{07}	x_{013}	x_{018}	(A)	-422.94
x_{03}	x_{08}	x_{014}	x_{019}	(V)	-755.98
x_{04}	x_{09}	x_{015}	x_{020}	(V)	579.33
x_{05}		x_{016}		(V)	635.88
Operation point magnitudes of a system with variable input voltage					
x_{010}	x_{011}	x_{021}	x_{022}	(V)	380.15
x_{01}	x_{06}	x_{012}	x_{017}	(A)	-308.29
x_{02}	x_{07}	x_{013}	x_{018}	(A)	-402.01
x_{03}	x_{08}	x_{014}	x_{019}	(V)	-718.59
x_{04}	x_{09}	x_{015}	x_{020}	(V)	551.08
x_{05}		x_{016}		(V)	604.65

$$\dot{x_{22}} = -\frac{(4\sqrt{x_{17}^2+x_{18}^2}-2x_{16}C'_{P4}\omega)}{\pi}\frac{x_{16}}{x_{22}}\frac{1}{C_{\mathrm{DL4}}} \tag{28e}$$

$$x_{a4} = \frac{1}{\pi C'_{\mathrm{P4}}\omega}(x_{17}\sin(\psi_4)^2 + x_{18}\mu_4) \tag{28f}$$

$$x_{b4} = \frac{1}{\pi C'_{\mathrm{P4}}\omega}(x_{18}\sin(\psi_4)^2 - x_{17}\mu_4) \tag{28g}$$

$$\cos\psi_4 = 1 - \frac{x_{16}C'_{P4}\omega}{\sqrt{x_{17}^2+x_{18}^2}} \tag{28h}$$

$$\mu_4 = \psi_4 - \sin_2(\psi_4)\cos(\psi_4). \tag{28i}$$

APPENDIX B

The derivation of the transfer functions of an IPOS system consisting of four SPRC-Bm with variable and fixed input voltage, $G_2(s), G_3(s)$, and $G_1(s)$, used for the controller design, is given in the following. After the linearization of the equations in Appendix A around a chosen operation point, given in Table V and by reintroducing the linearized state-space equations from (9)

$$\begin{aligned}\Delta\dot{x} &= \mathbf{A}\Delta x + \mathbf{B}\Delta u\\ \Delta y &= \mathbf{C}\Delta x + \mathbf{D}\Delta u\end{aligned} \tag{29}$$

the state vector Δx and the input vector Δu for an ISOP system with fixed input voltage are given as

$$\Delta x_{\mathrm{ISOP,fix}} = \left[\,\Delta x_1\,\Delta x_2\,\Delta x_3\,\Delta x_4\,\Delta x_5\,\Delta x_6\,\Delta x_7\,\Delta x_8\,\Delta x_9\,\right]^T$$

$$\Delta u_{\mathrm{ISOP,fix}} = \begin{bmatrix}\Delta D\\ \Delta\omega\\ \Delta V_{\mathrm{DL}}\\ \Delta D_2\\ \Delta\omega_2\\ \Delta V_{\mathrm{DL2}}\end{bmatrix}.$$

The system matrix $\mathbf{A}$ and the input matrix $\mathbf{B}$ are derived as

$$\mathbf{A}_{\mathrm{ISOP,fix}} = \begin{bmatrix} a_{11} & a_{12} & a_{13} & 0 & a_{15} & 0 & 0 & 0 & 0\\ a_{21} & a_{22} & 0 & a_{24} & a_{25} & 0 & 0 & 0 & 0\\ a_{31} & 0 & 0 & a_{34} & 0 & 0 & 0 & 0 & 0\\ 0 & a_{42} & a_{43} & 0 & 0 & 0 & 0 & 0 & 0\\ a_{51} & a_{52} & 0 & 0 & a_{55} & a_{56} & a_{57} & 0 & 0\\ 0 & 0 & 0 & 0 & a_{65} & a_{66} & a_{67} & a_{68} & 0\\ 0 & 0 & 0 & 0 & a_{75} & a_{76} & a_{77} & 0 & a_{79}\\ 0 & 0 & 0 & 0 & 0 & a_{86} & 0 & 0 & a_{89}\\ 0 & 0 & 0 & 0 & 0 & 0 & a_{97} & a_{98} & 0 \end{bmatrix}$$

$$\mathbf{B}_{\mathrm{ISOP,fix}} = \begin{bmatrix} b_{11} & b_{12} & b_{13} & 0 & 0 & 0\\ b_{21} & b_{22} & b_{23} & 0 & 0 & 0\\ 0 & b_{32} & 0 & 0 & 0 & 0\\ 0 & b_{42} & 0 & 0 & 0 & 0\\ 0 & b_{52} & 0 & 0 & b_{55} & 0\\ 0 & 0 & 0 & b_{64} & b_{65} & b_{66}\\ 0 & 0 & 0 & b_{74} & b_{75} & b_{76}\\ 0 & 0 & 0 & 0 & b_{85} & 0\\ 0 & 0 & 0 & 0 & b_{95} & 0 \end{bmatrix}.$$

It is assumed that all four SPRC-Bms have the same component values, therefore, $a_{11}=a_{66}$, $a_{12}=a_{67}$, $a_{13}=a_{68}$, $a_{15}=a_{65}$, $a_{21}=a_{76}$, $a_{22}=a_{77}$, $a_{24}=a_{79}$, $a_{25}=a_{75}$, $a_{31}=a_{86}$, $a_{34}=a_{89}$, $a_{42}=a_{97}$, $a_{43}=a_{98}$, $a_{51}=a_{56}$, $a_{52}=a_{57}$, and a_{55} is the coupling coefficient between both SPRC-Bms in the ISOP system. Also, $b_{11}=b_{64}$, $b_{12}=b_{65}$, $b_{13}=b_{66}$, $b_{21}=b_{74}$, $b_{22}=b_{75}$, $b_{23}=b_{76}$, $b_{32}=b_{85}$, $b_{42}=b_{95}$, and $b_{52}=b_{55}$.

The coefficients for the system matrix $\mathbf{A}$ are given below and the subindex $_0$ signals the corresponding operation point magnitude of the state and input variables

$$Z_1 = \sqrt{-\frac{x_{05}C_{\mathrm{P}}\omega_0 Z_3}{Z_5^{3/2}}} \tag{30}$$

$$Z_2 = Z_1\omega_0 x_{05}x_{01}(-C_{\mathrm{P}}Z_5^{3/2}\omega_0 x_{05} + Z_5^2) \tag{31}$$

$$Z_3 = x_{05}C_{\mathrm{P}}\omega_0\sqrt{Z_5} - 2Z_5 \tag{32}$$

$$Z_4 = \frac{\pi}{2} - \arcsin\left(-1 + \frac{x_{05}C_{\mathrm{P}}\omega_0}{\sqrt{Z_5}}\right) \tag{33}$$

$$Z_5 = x_{01}^2 + x_{02}^2 \tag{34}$$

$$Z_6 = \frac{Z_2}{L_S\pi C_P\omega_0^2 Z_5^3 x_{05} Z_3} - 2\frac{x_{01}Z_1}{L_S\pi C_P\omega_0 Z_5^2} \tag{35}$$

$$Z_7 = \frac{x_{05}x_{01}}{L_S\pi Z_5^{5/2} Z_1} - 2\frac{x_{01}Z_4}{L_S\pi C_P\omega_0 Z_5^2} \tag{36}$$

$$Z_8 = -\omega_0 Z_1(-C_P Z_5^{3/2}\omega_0 x_{05} Z_5 + x_{01}^6 + x_{02}^6 + 3Z_5 x_{01}^2 x_{02}^2) \tag{37}$$

$$Z_9 = -\frac{x_{05}}{L_S\pi\omega_0 {Z_5}^{3/2} Z_1} - \frac{Z_4}{L_S\pi C_P{\omega_0}^2 Z_5} \tag{38}$$

$$Z_{10} = \frac{Z_8\frac{x_{05}}{w_0}}{L_S\pi C_P{\omega_0}^2 {Z_5}^3 x_{05} Z_3} - \frac{Z_1}{L_S\pi C_P{\omega_0}^2 Z_5} \tag{39}$$

$$a_{11} = \frac{2x_{05}}{L_S\pi\sqrt{Z_5}}\left(\frac{x_{01}^2}{Z_5} - 1\right) + \frac{C_P\omega_0 x_{05}^2}{Z_5 L_S\pi}\left(1 - \frac{2x_{01}^2}{Z_5}\right) - \frac{r}{L_S} + \frac{Z_2 x_{02}}{L_S\pi Z_5^2\omega_0 Z_3}\left(-\frac{1}{\sqrt{Z_5}} + \frac{1}{C_P\omega_0 x_{05}}\right) + \frac{x_{02}x_{05}x_{01}}{L_S\pi {Z_5}^{3/2}}\left(Z_1 + \frac{1}{Z_1}\right) \tag{40}$$

$$a_{12} = \frac{x_{05}}{L_S\pi Z_5^{3/2}}\left[2x_{02}x_{01} - Z_1 Z_5 + x_{02}^2\left(\frac{1}{Z_1} + Z_1 - 2\frac{C_P\omega_0 x_{01}x_{05}}{\sqrt{Z_5}x_{02}}\right)\right] + \frac{-\pi + Z_1 + Z_4}{L_S C_P\pi\omega_0} + \omega_0 + \frac{Z_2\frac{x_{02}^2}{x_{01}}\left(\sqrt{Z_5} - C_P\omega_0 x_{05}\right)}{L_S\pi C_P\omega_0^2 Z_5^{5/2} x_{05} Z_3} \tag{41}$$

$$a_{13} = a_{24} = \frac{-1}{L_S} \tag{42}$$

$$a_{15} = \frac{C_P\omega_0 x_{01}x_{05}}{0.5 L_S\pi Z_5} - \frac{2x_{01} + x_{02}Z_1 + \frac{x_{02}}{Z_1}}{L_S\pi\sqrt{Z_5}} + \frac{x_{02}Z_8(\sqrt{Z_5} - x_{05}\omega_0 C_P)}{L_S\pi C_P\omega_0^2 Z_5^{5/2} x_{05} Z_3} \tag{43}$$

$$a_{21} = \frac{-C_P\omega_0 x_{01}x_{05}^2 x_{02}}{0.5 L_S\pi Z_5^2} - x_{01}Z_5(Z_6 + Z_7) - \omega_0 + \frac{x_{01}^2 x_{05}\left(\frac{2x_{02}}{x_{01}} - Z_1\right)}{L_S\pi Z_5^{3/2}} + \frac{Z_1 x_{05}}{L_S\pi\sqrt{Z_5}} + \frac{Z_2 x_{01}}{L_S\pi Z_5^{5/2}\omega_0 Z_3} + \frac{(\pi - Z_4 - Z_1)(Z_5 + 2x_{01}^2) - 2\pi x_{01}^2}{L_S\pi C_P\omega_0 Z_5} \tag{44}$$

$$a_{22} = \frac{x_{05}^2 C_P\omega_0}{L_S\pi Z_5}\left(1 - \frac{2x_{02}^2}{Z_5}\right) - x_{02}Z_5(Z_6 + Z_7) + \frac{Z_3 x_{02}}{L_S\pi Z_5^{5/2}\omega_0 Z_3} + \frac{x_{05}(2x_{02}^2 - x_{02}Z_1 x_{01} - 2Z_5)}{L_S\pi Z_5^{3/2}} - \frac{2x_{02}x_{01}(Z_1 + Z_4)}{L_S C_P\pi\omega_0 Z_5} - \frac{r}{L_S} \tag{45}$$

$$a_{25} = \frac{Z_1 x_{01} + \frac{x_{01}}{Z_1} - 2x_{02}}{L_S\pi\sqrt{Z_5}} - \frac{Z_8 x_{01}(Z_5 - \omega_0 C_P\sqrt{Z_5}x_{05})}{L_S\pi C_P\omega_0^2 Z_5^3 x_{05} Z_3} + \frac{C_P\omega_0 x_{02}x_{05}}{0.5 L_S\pi Z_5} \tag{46}$$

$$a_{31} = a_{42} = \frac{1}{C_S} \tag{47}$$

$$a_{34} = -a_{43} = \omega_0 \tag{48}$$

$$a_{51} = \frac{4x_{01}}{C_f\sqrt{Z_5}\pi} \tag{49}$$

$$a_{52} = \frac{4x_{02}}{C_f\sqrt{Z_5}\pi} \tag{50}$$

$$a_{55} = \frac{1}{C_f}\left(-\frac{1}{R_L} - 2\frac{C_P\omega_0}{\pi} - 2\frac{C_{P2}\omega_{02}}{\pi}\right). \tag{51}$$

Next, the coefficients for the input matrix $\mathbf{B}$ are given below

$$b_{11} = \frac{V_{DL0}\cos(D_0\pi)}{L_S} \tag{52}$$

$$b_{12} = \frac{C_P x_{01}x_{05}^2}{L_S\pi Z_5} - \frac{x_{02}Z_8(\omega_0 x_{05}C_P - \sqrt{Z_5})}{L_S\pi C_P Z_5^{5/2}\omega_0^3 Z_3} + \frac{x_{02}(\pi - Z_4 - Z_1)}{L_S\pi C_P\omega_0^2} - \frac{x_{02}x_{05}}{L_S\pi\omega_0\sqrt{Z_5}Z_1} + x_{02} \tag{53}$$

$$b_{13} = \frac{\sin(D_0\pi)}{L_S\pi} \tag{54}$$

$$b_{21} = -\frac{V_{DL0}\sin(D_0\pi)}{L_S} \tag{55}$$

$$b_{22} = \frac{C_P x_{02}x_{05}^2}{L_S\pi Z_5} - x_{01}Z_5(Z_9 + Z_{10}) - x_{01} + \frac{Z_8 x_{05}x_{01}}{L_S\pi Z_5^{5/2}\omega_0^2 Z_3} - \frac{x_{01}}{L_S C_P\omega_0^2} \tag{56}$$

$$b_{23} = \frac{\cos(D_0\pi) - 1}{L_S\pi} \tag{57}$$

$$b_{32} = x_{04} \tag{58}$$

$$b_{42} = -x_{03} \tag{59}$$

$$b_{52} = -\frac{2x_{05}C_P}{C_f\pi}. \tag{60}$$

For an ISOP system with variable input voltage the state and the input vector are written as

$$\Delta x_{\text{ISOP,var}} = \left[\,[\Delta x_{\text{ISOP,fix}}]^T\ \Delta x_{10}\ \Delta x_{11}\,\right]^T$$

$$\Delta u_{\text{ISOP,var}} = \begin{bmatrix}\Delta D\\ \Delta\omega\\ \Delta D_2\\ \Delta\omega_2\end{bmatrix}$$

where the input vector $\Delta x_{\text{ISOP,var}}$ is composed of $\Delta x_{\text{ISOP,fix}}$ and the variable input voltages Δx_{10} and Δx_{11}. The input vector

$\Delta u_{\text{ISOP,var}}$ is reduced to four inputs. Also the system matrix $\mathbf{A}_{\text{ISOP,var}}$ contains $\mathbf{A}_{\text{ISOP,fix}}$ with identical coefficients and is derived as

$$\mathbf{A}_{\text{ISOP,var}} = \begin{bmatrix} \begin{bmatrix} & & \\ & \mathbf{A}_{\text{ISOP,fix}} & \\ & & \end{bmatrix} & \begin{matrix} a_{110} & 0 \\ a_{210} & 0 \\ 0 & 0 \\ 0 & 0 \\ 0 & 0 \\ 0 & a_{611} \\ 0 & a_{711} \\ 0 & 0 \\ 0 & 0 \end{matrix} \\ \begin{matrix} a_{101} & a_{102} & 0 & 0 & a_{105} & 0 & 0 & 0 & 0 \\ 0 & 0 & 0 & 0 & a_{115} & a_{116} & a_{117} & 0 & 0 \end{matrix} & \begin{matrix} a_{1010} & 0 \\ 0 & a_{1111} \end{matrix} \end{bmatrix}.$$

The additional coefficients of $\mathbf{A}_{\text{ISOP,var}}$ are

$$a_{101} = -4\frac{x_{01}x_{05}}{\sqrt{Z_5}\pi x_{010}C_{\text{DL1}}} \tag{61}$$

$$a_{102} = -4\frac{x_{02}x_{05}}{\sqrt{Z_5}\pi x_{010}C_{\text{DL1}}} \tag{62}$$

$$a_{105} = -4\frac{(\sqrt{Z_5} - x_{05}C_{\text{P}}\omega_0)}{x_{010}C_{\text{DL1}}\pi} \tag{63}$$

$$a_{1010} = -2\frac{\left(x_{05}C_{\text{P}}\omega_0 - 2\sqrt{Z_5}\right)x_{05}}{\pi {x_{010}}^2 C_{\text{DL1}}} \tag{64}$$

$$a_{110} = \frac{\sin(D_0\pi)}{L_{\text{S}}\pi} \tag{65}$$

$$a_{210} = \frac{\cos(D_0\pi) - 1}{L_{\text{S}}\pi} \tag{66}$$

with $a_{110} = a_{611}$, $a_{210} = a_{711}$, $a_{101} = a_{116}$, $a_{102} = a_{117}$, $a_{105} = a_{115}$, and $a_{1010} = a_{1111}$.

The input matrix $\mathbf{B}_{\text{ISOP,var}}$ is given as

$$\mathbf{B}_{\text{ISOP,var}} = \begin{bmatrix} b_{11} & b_{12} & 0 & 0 \\ b_{21} & b_{22} & 0 & 0 \\ 0 & b_{32} & 0 & 0 \\ 0 & b_{42} & 0 & 0 \\ 0 & b_{52} & 0 & b_{54} \\ 0 & 0 & b_{63} & b_{64} \\ 0 & 0 & b_{73} & b_{74} \\ 0 & 0 & 0 & b_{84} \\ 0 & 0 & 0 & b_{94} \\ 0 & b_{102} & 0 & 0 \\ 0 & 0 & 0 & b_{114} \end{bmatrix}$$

where the coefficients $b_{11}, b_{12}, b_{21}, b_{22}, b_{32}, b_{42}$, and b_{52} are the same as the coefficients of the matrix $\mathbf{B}_{\text{ISOP,fix}}$, unless in b_{11} and b_{21}, V_{DL0} is replaced by x_{010}. Within the matrix $\mathbf{B}_{\text{ISOP,var}}$, the coefficients are $b_{11} = b_{63}$, $b_{12} = b_{64}$, $b_{21} = b_{73}$, $b_{22} = b_{74}$, $b_{32} = b_{84}$, $b_{42} = b_{94}$, $b_{52} = b_{54}$, and $b_{102} = b_{114}$ with

$$b_{102} = \frac{2x_{05}^2 C_{\text{P}}}{\pi x_{010}C_{\text{DL1}}}. \tag{67}$$

Finally, the state-space representation of the IPOS system either with fixed or variable input voltage is given with the state vector

$$\Delta x_{\text{IPOS}} = \left[\, [\Delta x_{\text{ISOP1}}]^T \; [\Delta x_{\text{ISOP2}}]^T \,\right]^T$$

and the input vector

$$\Delta u_{\text{IPOS}} = \left[\, [\Delta u_{\text{ISOP1}}]^T \; [\Delta u_{\text{ISOP2}}]^T \,\right]^T.$$

The state matrix $\mathbf{A}_{\text{IPOS}}$ is formed by the two ISOP state matrices in the diagonal and the coefficients

$$a_{514} = -\frac{1}{C_{\text{f}}R_{\text{L}}} \tag{68}$$

and

$$a_{145} = -\frac{1}{C_{f2}R_{\text{L}}} \tag{69}$$

if an ISOP with fixed input voltage is considered. If an ISOP with variable input voltage is considered, $a_{514} \rightarrow a_{516}$ and $a_{145} \rightarrow a_{165}$, calculated with (68) and (69). The rest of the matrix is filled with zeros. The coefficients a_{514}, a_{145}, a_{516}, and a_{165} represent the series output connection of the ISOP systems

$$\mathbf{A}_{\text{IPOS}} = \begin{bmatrix} \begin{bmatrix} & \\ \mathbf{A}_{\text{ISOP1}} & \\ & \end{bmatrix} & \begin{bmatrix} 0 & \cdots & 0 \\ \vdots & a_{514}, & \vdots \\ & a_{516} & \\ 0 & \cdots & 0 \end{bmatrix} \\ \begin{bmatrix} 0 & \cdots & 0 \\ \vdots & a_{145}, & \vdots \\ & a_{165} & \\ 0 & \cdots & 0 \end{bmatrix} & \begin{bmatrix} & \\ \mathbf{A}_{\text{ISOP2}} & \\ & \end{bmatrix} \end{bmatrix}.$$

The input matrix $\mathbf{B}_{\text{IPOS}}$ is formed by the two ISOP input matrices in the diagonal and zeros elsewhere

$$\mathbf{B}_{\text{IPOS}} = \begin{bmatrix} \begin{bmatrix} \\ \mathbf{B}_{\text{ISOP1}} \\ \end{bmatrix} & \begin{bmatrix} \\ \mathbf{0} \\ \end{bmatrix} \\ \begin{bmatrix} \\ \mathbf{0} \\ \end{bmatrix} & \begin{bmatrix} \\ \mathbf{B}_{\text{ISOP2}} \\ \end{bmatrix} \end{bmatrix}.$$

The output voltage and the RMS resonant currents are the output equations of the fixed input voltage ISOP system

$$y_{1,\text{fix}} = x_5 \cdot \ddot{u} = V_{O1} \cdot \ddot{u} \tag{70}$$

$$y_{2,\text{fix}} = \sqrt{2(x_1^2 + x_2^2)} = I_{\text{res1,RMS}} \tag{71}$$

$$y_{3,\text{fix}} = \sqrt{2(x_6^2 + x_7^2)} = I_{\text{res2,RMS}} \tag{72}$$

with $\ddot{u} = 20$, which is the transformers ratio. After the linearization of (70), (71), and (72), the output matrix $\mathbf{C_{IPOS,fix}}$ of the IPOS system is given as

$$\mathbf{C_{IPOS,fix}} = \left[\begin{bmatrix} 0 & 0 & 0 & 0 & \ddot{u} & 0 & 0 & 0 & 0 \\ c_{21} & c_{22} & 0 & 0 & 0 & 0 & 0 & 0 & 0 \\ 0 & 0 & 0 & 0 & 0 & c_{36} & c_{37} & 0 & 0 \end{bmatrix}, \begin{bmatrix} 0 \\ \mathbf{3 \times 9} \\ 0 \end{bmatrix}\right]$$

with the coefficients

$$c_{21} = \frac{\sqrt{2}x_{01}}{\sqrt{x_{01}^2 + x_{02}^2}} \tag{73}$$

$$c_{22} = \frac{\sqrt{2}x_{02}}{\sqrt{x_{01}^2 + x_{02}^2}} \tag{74}$$

where $c_{36} = c_{21}$ and $c_{37} = c_{22}$, due to the same component values of all SPRC Bms. The output equations of the IPOS with variable input voltages are

$$y_{1,\text{var}} = x_{10} = V_{\text{DL1}} \tag{75}$$

$$y_{2,\text{var}} = x_{11} = V_{\text{DL2}} \tag{76}$$

leading to the output matrix $\mathbf{C_{IPOS,var}}$ of the IPOS system

$$\mathbf{C_{IPOS,var}} = \left[\begin{bmatrix} 0 & 0 & 0 & 0 & 0 & 0 & 0 & 0 & 0 & 1 & 0 \\ 0 & 0 & 0 & 0 & 0 & 0 & 0 & 0 & 0 & 0 & 1 \end{bmatrix}, \begin{bmatrix} \mathbf{0} \\ \mathbf{2 \times 11} \end{bmatrix}\right].$$

Reintroducing

$$G_2(s) = -G_{\text{Bm1},\Delta\text{VDL1}}(s) + G_{\text{Bm2},\Delta\text{VDL1}}(s) + \\ + G_{\text{Bm1},\Delta\text{VDL2}}(s) - G_{\text{Bm2},\Delta\text{VDL2}}(s) \tag{77}$$

and using the state-space equations of the variable input voltage IPOS system the transfer functions forming $G_2(s)$ are derived as

$$G_{\text{Bm1},\Delta\text{VDL1}}(s) = \left.\frac{\Delta V_{\text{DL1}}}{\Delta D}\right|_{\Delta\omega,\Delta D_2,\Delta\omega_2=0} \tag{78}$$

$$G_{\text{Bm2},\Delta\text{VDL1}}(s) = \left.\frac{\Delta V_{\text{DL1}}}{\Delta D_2}\right|_{\Delta D,\Delta\omega,\Delta\omega_2=0} \tag{79}$$

$$G_{\text{Bm1},\Delta\text{VDL2}}(s) = \left.\frac{\Delta V_{\text{DL2}}}{\Delta D}\right|_{\Delta\omega,\Delta D_2,\Delta\omega_2=0} \tag{80}$$

$$G_{\text{Bm2},\Delta\text{VDL2}}(s) = \left.\frac{\Delta V_{\text{DL2}}}{\Delta D_2}\right|_{\Delta D,\Delta\omega,\Delta\omega_2=0}. \tag{81}$$

Using the state-space equations of the IPOS system with fixed input voltage, the transfer functions forming $G_3(s)$

$$G_3(s) = G_{\text{Bm1},\Delta\text{VO1}}(s) + G_{\text{Bm2},\Delta\text{VO1}}(s) \tag{82}$$

and $G_1(s)$

$$G_1(s) = [G_{\text{Bm1},\Delta\text{Ires1}}(s) + G_{\text{Bm2},\Delta\text{Ires1}}(s) + \\ G_{\text{Bm1},\Delta\text{Ires2}}(s) + G_{\text{Bm2},\Delta\text{Ires2}}(s)] \cdot H_1 \tag{83}$$

TABLE VI
NOMINATOR AND DENOMINATOR COEFFICIENTS IN S-DOMAIN OF THE TRANSFER FUNCTIONS

$G_1(s)$			
	$Z(s)$		$N(s)$
b_0	347.858141666217 E30	a_0	320.874817640644 E27
b_1	87.8086792032053 E27	a_1	99.7921833632613 E24
b_2	5.08050633578414 E24	a_2	8.26581530811099 E21
b_3	−94.1273080386993 E18	a_3	165.063231946826 E15
b_6	7.48114064263216 E12	a_4	1.35900330214233 E12
b_5	129.640460164061 E06	a_5	222.894213465120 E03
b_6	0	a_6	1
$G_2(s)$			
	$Z(s)$		$N(s)$
b_0	10.1212247856719 E27	a_0	3.79065890642367 E24
b_1	182.008775742464 E24	a_1	827.226019150503 E21
b_2	8.52047738455378 E21	a_2	13.6251584893958 E21
b_3	−1.06934095719994 E15	a_3	135.072774356601 E15
b_6	11.7186228653460 E09	a_4	1.37063207938328 E12
b_5	0	a_5	185.741250905273 E03
b_6	0	a_6	1
$G_3(s)$			
	$Z(s)$		$N(s)$
b_0	329.836149464061 E33	a_0	12.9421960277760 E30
b_1	23.0516073912384 E30	a_1	1.76733652416190 E27
b_2	421.040002120177 E24	a_2	43.7851209147386 E21
b_3	−34.4322590784590 E18	a_3	461.534766030359 E15
b_6	581.373641944023 E12	a_4	1.40764795593576 E12
b_5	292.448439615617 E03	a_5	441.215443874179 E03
b_6	0	a_6	1

are given as

$$G_{\text{Bm1},\Delta\text{VO1}}(s) = \left.\frac{\Delta V_{O1}}{\Delta D}\right|_{\Delta\omega,\Delta V_{\text{DL1}},\Delta D_2,\Delta\omega_2,\Delta V_{\text{DL2}}=0} \tag{84}$$

$$G_{\text{Bm2},\Delta\text{VO1}}(s) = \left.\frac{\Delta V_{O1}}{\Delta D_2}\right|_{\Delta D,\Delta\omega,\Delta V_{\text{DL1}},\Delta\omega_2,\Delta V_{\text{DL2}}=0} \tag{85}$$

respectively

$$G_{\text{Bm1},\Delta\text{Ires1}}(s) = \left.\frac{\Delta I_{\text{res1,RMS}}}{\Delta D}\right|_{\Delta\omega,\Delta V_{\text{DL1}},\Delta D_2,\Delta\omega_2,\Delta V_{\text{DL2}}=0} \tag{86}$$

$$G_{\text{Bm2},\Delta\text{Ires1}}(s) = \left.\frac{\Delta I_{\text{res1,RMS}}}{\Delta D_2}\right|_{\Delta D,\Delta\omega,\Delta V_{\text{DL1}},\Delta\omega_2,\Delta V_{\text{DL2}}=0} \tag{87}$$

$$G_{\text{Bm1},\Delta\text{Ires2}}(s) = \left.\frac{\Delta I_{\text{res2,RMS}}}{\Delta D}\right|_{\Delta\omega,\Delta V_G,\Delta D_2,\Delta\omega_2,\Delta V_{\text{DL2}}=0} \tag{88}$$

$$G_{\text{Bm2},\Delta\text{Ires2}}(s) = \left.\frac{\Delta I_{\text{res2,RMS}}}{\Delta D_2}\right|_{\Delta D,\Delta\omega,\Delta V_{\text{DL1}},\Delta\omega_2,\Delta V_{\text{DL2}}=0} \tag{89}$$

Finally, the coefficients used in

$$G(s) = \frac{Z(s)}{N(s)} = \frac{b_m s^m + b_{m-1}s^{m-1} + \ldots + b_1 s + b_0}{a_n s^n + a_{n-1}s^{n-1} + \ldots + a_1 s + a_0} \tag{90}$$

which forms the transfer functions $G_1(s)$, $G_2(s)$, and $G_3(s)$ are given as a balanced realization [25] in Table VI.

REFERENCES

[1] H. Pfeffer *et al.*, "A long pulse modulator for reduced size and cost," in *Proc. Conf. Power Modulator Symp.*, 1994, pp. 48–51.

[2] J. S. Bakken, "Study and development of solid state based long pulse klystron modulators for future linear accelerators at CERN," Institutt for elkraftteknikk, 2007.

[3] M. Jaritz and J. Biela, "Optimal design of a modular series parallel resonant converter for a solid state 2.88 MW/115-kV long pulse modulator," *IEEE Trans. Plasma Sci.*, vol. 42, no. 10, pp. 3014–3022, Oct. 2014.

[4] G. Ivensky, A. Kats, and S. Ben-Yaakov, "A novel RC model of capacitive-loaded parallel and series-parallel resonant DC-DC converters," in *Proc. IEEE Power Electron. Spec. Conf.*, 1997, vol. 2, pp. 958–964.

[5] G. Ivensky, A. Kats, and S. Ben-Yaakov, "An RC load model of parallel and series-parallel resonant DC-DC converters with capacitive output filter," *IEEE Trans. Power Electron.*, vol. 14, no. 3, pp. 515–521, May 1999.

[6] M. Jaritz, S. Blume, and J. Biela, "Design procedure of a 14.4 kV, 100 kHz transformer with a high isolation voltage (115 kV)," *IEEE Trans. Dielect. Elect. Insul.*, vol. 24, no. 4, pp. 2094–2104, Sept. 2017.

[7] M. Jaritz, A. Hillers, and J. Biela, "General analytical model for the thermal resistance of windings made of solid or Litz wire," *IEEE Trans. Power Electron.,* to be published.

[8] R. Giri, V. Choudhary, R. Ayyanar, and N. Mohan, "Common-duty-ratio control of input-series connected modular DC-DC converters with active input voltage and load-current sharing," *IEEE Trans. Ind. Appl.*, vol. 42, no. 4, pp. 1101–1111, Jul. 2006.

[9] J.-W. Kim, J.-S. Yon, and B. Cho, "Modeling, control, and design of input-series-output-parallel-connected converter for high-speed-train power system," *IEEE Trans. Ind. Electron*, , vol. 48, no. 3, pp. 536–544, Jun. 2001.

[10] R. Ayyanar, R. Giri, and N. Mohan, "Active input-voltage and load-current sharing in input-series and output-parallel connected modular DC-DC converters using dynamic input-voltage reference scheme," *IEEE Trans. Power Electron.*, vol. 19, no. 6, pp. 1462–1473, Nov. 2004.

[11] X. Ruan, W. Chen, L. Cheng, C. Tse, H. Yan, and T. Zhang, "Control strategy for input-series-output-parallel converters," *IEEE Trans. Ind. Electron.*, vol. 56, no. 4, pp. 1174–1185, Apr. 2009.

[12] W. Chen, X. Ruan, H. Yan, and C. Tse, "DC/DC conversion systems consisting of multiple converter modules: Stability, control, and experimental verifications," *IEEE Trans. Power Electron.*, vol. 24, no. 6, pp. 1463–1474, Jun. 2009.

[13] W. Chen and X. Ruan, "Modularization structure for series-parallel connected converters," in *Proc. 23rd Annu. IEEE Appl. Power Electron. Conf. Expo.*, Feb. 2008, pp. 1531–1535.

[14] K. Siri, K. Conner, and C. Truong, "Uniform voltage distribution control for paralleled-input, series-output connected converters," in *Proc. IEEE Aerosp. Conf.*, Mar. 2005, pp. 1–11.

[15] S. Manias and G. Kostakis, "Modular dc–dc convertor for high-output voltage applications," *IEE Proc. B—Elect. Power Appl.*, vol. 140, no. 2, pp. 97–102, Mar. 1993.

[16] J. Martin-Ramos, J. Diaz, A. Pernia, J. Lopera, and F. Nuno, "Dynamic and steady-state models for the PRC-LCC resonant topology with a capacitor as output filter," *IEEE Trans. Ind. Electron.*, vol. 54, no. 4, pp. 2262–2275, Aug. 2007.

[17] J. Martin-Ramos, A. Pernia, J. Diaz, F. Nuno, and J. Alonso, "A circuit for the large and small signal dynamic modeling of the PRC-LCC resonant topology with a capacitor as output filter," in *Proc. IEEE Power Electron. Spec. Conf.*, Jun. 2005, pp. 635–641.

[18] J. A. Martin-Ramos, A. M. Pernía, J. Díaz, F. Nuno, and J. A. Martinez, "Power supply for a high-voltage application," *IEEE Trans. Power Electron.*, vol. 23, no. 4, pp. 1608–1619, Jul. 2008.

[19] E. X. Yang, F. C. Lee, and M. Jovanovic, "Mall-signal modeling of power electronic circuits using extended describing function technique," in *Proc. Virginia Power Electron. Semin.*, 1991, vol. 4, pp. 155–166.

[20] F. S. Cavalcante and J. W. Kolar, "Small-signal model of a 5kW high-output voltage capacitive-loaded series-parallel resonant DC-DC converter," in *Proc. 36th IEEE Proc. Power Electron. Spec. Conf.*, 2005, pp. 1271–1277.

[21] M. Z. Youssef and P. K. Jain, "A review and performance evaluation of control techniques in resonant converters," in *Proc. 30th Annu. IEEE Ind. Electron. Soc. Conf.*, Nov. 2004, vol. 1, pp. 215–221.

[22] M. Jaritz, T. Rogg, and J. Biela, "Control of a modular series parallel resonant converter system for a solid state 2.88MW/115-kV long pulse modulator," in *Proc. 17th Eur. IEEE Power Electron. Appl. Conf.*, Sep. 2015, pp. 1–11.

[23] H. Yan, X. Ruan, and W. Chen, "The input voltage sharing control strategy for input-series and output-parallel converter under extreme conditions," in *Proc. Energy Convers. Congr. Expo.*, Sep. 2009, pp. 662–667.

[24] A. von Jouanne, S. Dai, and H. Zhang, "A multilevel inverter approach providing DC-link balancing, ride-through enhancement, and common-mode voltage elimination," *IEEE Trans. Ind. Electron.*, vol. 49, no. 4, pp. 739–745, Aug. 2002.

[25] O. Föllinger, F. Dörrscheidt, and M. Klittich, *Regelungstechnik*, 10th ed. Heidelberg, Germany: Hüthig, 2008.

Michael Jaritz (M'17) was born in Graz, Austria, in 1984. He received the Dipl.-Ing. degree in electrical engineering from the Technical University of Graz, Graz, Austria, in 2010.

His diploma thesis dealt with dc voltage link inverters in a power range of 500 kW. Since September 2011, he has been with the High Power Electronics Laboratory, ETH-Zürich, Zürich, Switzerland as a Ph.D. student. There he is focusing on series-parallel resonant converters that are used in long pulse modulators generating highly accurate voltage pulses.

Tobias Rogg received the Electrical Engineering and Information Technology degree from the Karlsruhe Institute of Technology, Karlsruhe, Germany, specializing in power electronics and electrical drives, the Master's degree in Karlsruhe Institute of Technology (with distinction), in 2014, and the Ph.D. degree focusing on converter systems for traction applications from High Power Electronics Laboratory, ETH-Zürich, Zürich, Switzerland.

At the University of Southampton, he dealt with energy systems as an exchange student. As part of his Master's thesis, he developed a self-commissioning procedure to estimate the flux linkage of the nonlinear synchronous reluctance machine at ABB Corporate Research in Västerås, Sweden.

Juergen Biela (S'04–M'06–SM'16) received the Diploma (Hons.) degree from Friedrich-Alexander-Universitaet, Erlangen-Nuernberg, Germany, and the Ph.D. degree from the Swiss Federal Institute of Technology (ETH Zurich), Zürich, Switzerland, in 1999 and 2006, respectively.

He dealt, in particular, with resonant dc-link inverters with the University of Strathclyde, Glasgow, U.K., and the active control of series-connected IGCTs with the Technical University of Munich, Munich, Germany, during his studies. In 2000, he joined the Research Department of Siemens Automation and Drives, Erlangen, Germany, where he was involved in inverters with very high switching frequencies, SiC components, and EMC. In 2002, he joined the Power Electronic Systems Laboratory (PES), ETH Zurich, for working toward the Ph.D. degree, focusing on optimized electromagnetically integrated resonant converters. From 2006 to 2007, he was a Postdoctoral Fellow with PES and a Guest Researcher with the Tokyo Institute of Technology, Tokyo, Japan. From 2007 to 2010, he was a Senior Research Associate with PES. Since 2010, he has been an Associate Professor in high-power electronic systems with ETH Zurich. His current research interests include the design, modeling, and optimization of PFC, dcdc and multilevel converters with emphasis on passive components, and the design of pulsed-power systems and power electronic systems for future energy distribution.